

electronic reprint

## International Tables for Crystallography

### Volume H: Powder diffraction

Edited by C. J. Gilmore, J. A. Kaduk and H. Schenk

Chapter 5.8. Scattering methods for disordered heterogeneous materials

A. J. Allen

Author(s) of this chapter may load this reprint on their own web site or institutional repository provided that this cover page is retained. Republication of this chapter or its storage in electronic databases other than as specified above is not permitted without prior permission in writing from the IUCr.



International Tables **Online** is available from [it.iucr.org](http://it.iucr.org)

## 5.8. Scattering methods for disordered heterogeneous materials

A. J. ALLEN

### 5.8.1. Introduction and overview

#### 5.8.1.1. Amorphous and non-crystalline materials

While powder diffraction and single-crystal diffraction have long comprised the standard means for determining the structure, phase and even the composition of solid materials, standard powder or single-crystal diffraction methods cannot be applied if no (or little) crystalline structure is present. The most obvious examples of amorphous and non-crystalline solid materials are glasses, polymers, various types of gel and sometimes thin films. A uniform amorphous material without structure at any length scale would not be very tractable to diffraction-based measurements of almost any kind. Fortunately, only a few (if any) materials amorphous over all length scales exist in nature. Most so-called amorphous materials contain some short-range order that can be elucidated, at least to some extent, by wide-angle liquid- or total-scattering methods increasingly available at synchrotron X-ray or neutron scattering facilities. Such methods are also applicable to

poorly crystalline solids where defects and other heterogeneities disrupt any long-range order, and also to nanocrystalline materials where the crystal structure order is short range by definition (Bates *et al.*, 2006). Since wide-angle scattering (WAS) methods in general, and nanocrystalline materials in particular, are covered elsewhere in this volume (see Chapters 5.6 and 5.7), they will be discussed fairly briefly in this chapter. Here we will focus more on the disorder and heterogeneity at the microstructural level (from  $\sim 10$  Å to several  $\mu\text{m}$ ), which pervades all material systems (including thin films) that are not uniform in structure and composition across all length scales.

#### 5.8.1.2. Disordered and heterogeneous (and multi-component) materials

Fig. 5.8.1 presents examples of measurements possible for disordered and heterogeneous materials, together with the scale ranges applicable to the techniques discussed.

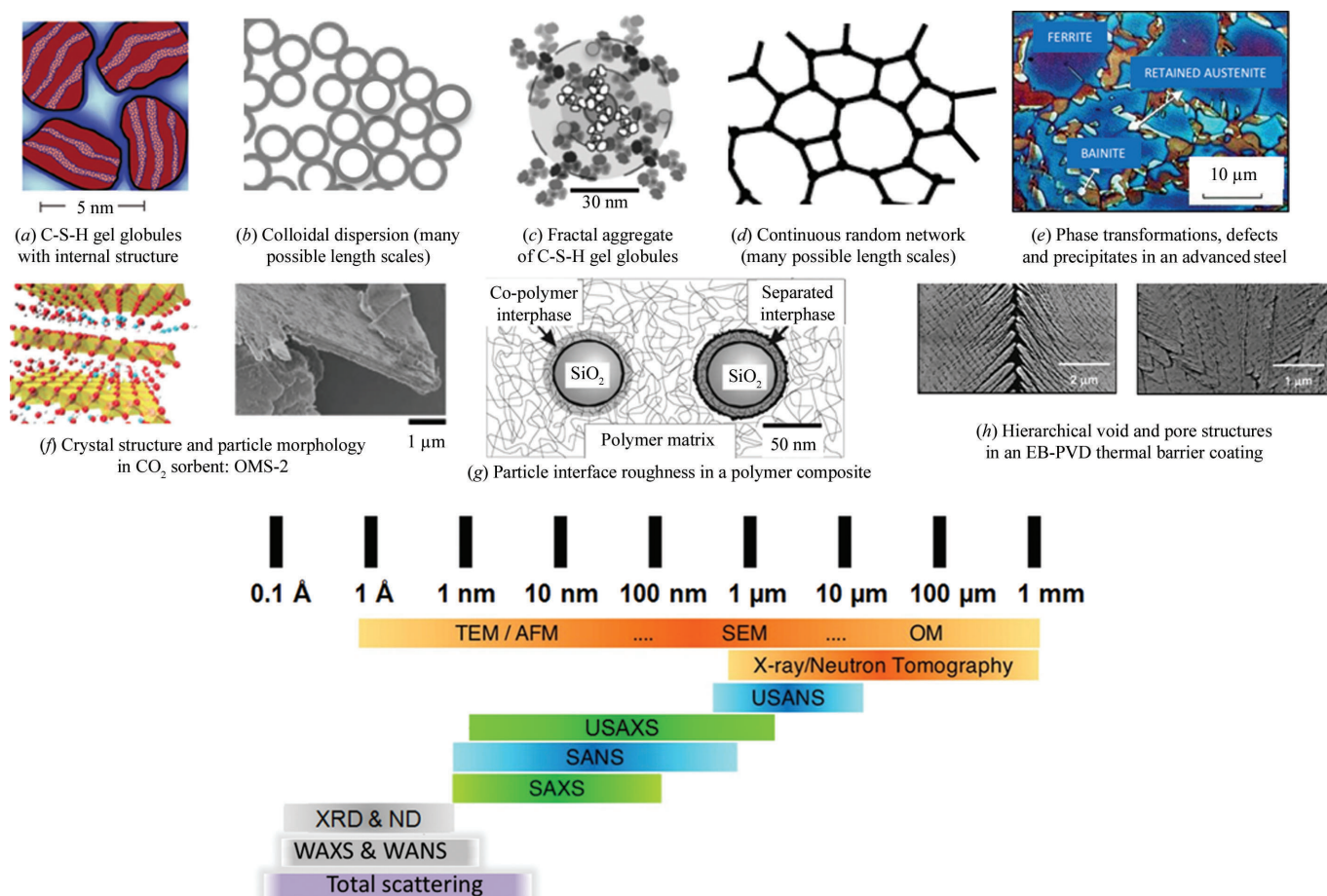


**Figure 5.8.1**

Examples of scattering methods applied to disordered, heterogeneous materials, together with the scale ranges of interest and the applicable scattering-based methods. Material examples: (a) calcium-silicate hydrate (C-S-H) gel globules in hydrating cement (Allen *et al.*, 2007); (b) colloidal particle dispersion (Bates *et al.*, 2006); (c) fractal aggregate of C-S-H gel globules (Jennings, 2000); (d) continuous random network [as (b)]; (e) complex microstructure of an advanced steel; (f) crystal layer structure and associated lamellar morphology of  $\text{CO}_2$  solid sorbent, OMS-2 (Espinal *et al.*, 2012); (g) interphase-controlled interface surface roughness between particles and matrix in a polymer composite (Wilson *et al.*, 2007); and (h) void/pore structures in an electron-beam physical vapour-deposited (EB-PVD) thermal barrier coating (Renteria *et al.*, 2007). Techniques: TEM and SEM = transmission and scanning electron microscopy, AFM = atomic force microscopy, OM = optical microscopy (microscopies and imaging included for comparison); SAXS and SANS, USAXS and USANS = small-angle and ultra-small-angle X-ray and neutron scattering; XRD and ND = X-ray and neutron diffraction (structure determination); WAXS and WANS = wide-angle X-ray and neutron scattering (phase analysis, diffuse-scattering effects); and total scattering (atomic pair distribution function analysis).

## 5. DEFECTS, TEXTURE AND MICROSTRUCTURE

**Table 5.8.1**

Information on disordered or heterogeneous material systems using scattering methods

Abbreviations: GI-SAXS = grazing-incidence SAXS, NS-SANS = near-surface SANS, XRR = X-ray reflectivity, NR = neutron reflectivity.

| $Q$ -range, obtainable information<br>(examples or applications)   | SAXS,<br>SANS | USAXS,<br>USANS | GI-SAXS,<br>NS-SANS | XRR,<br>NR     | WAXS,<br>WANS | Total<br>scattering |
|--|---------------|-----------------|---------------------|----------------|---------------|---------------------|
| Minimum $Q$ ( $\text{\AA}^{-1}$ )  | $10^{-3}$     | $< 10^{-4}$     | $10^{-3}$           | $\sim 10^{-1}$ | 1             | $\sim 1$            |
| Maximum $Q$ ( $\text{\AA}^{-1}$ )  | 1             | 1 or $10^{-3}$  | 1                   | $> 1$          | $\sim 5$      | $> 40$              |
| Lattice spacings, crystal phases<br>(precipitates/minority phases in alloys, CO <sub>2</sub> solid sorbents)         |               |                 |                     |                | ×             | ×                   |
| Mean particle or pore size, shape<br>(colloids, porous rocks)  | ×             | ×               | ×                   | ×              |               |                     |
| Size distribution<br>(precipitate nucleation, growth and coarsening)   | ×             | ×               | ×                   |                |               |                     |
| Pore or particle volume fraction<br>(solution-mediated particle formation, cement hydration)                         | ×             | ×               |                     |                |               |                     |
| Pore, particle or interface surface area and roughness<br>(coating de-lamination, composite particle/matrix bonding) | ×             | ×               | ×                   | ×              |               |                     |
| Composition, density of solid phases or layers<br>(deposited dielectric films, clays, catalysts)                     | ×             | ×               | ×                   | ×              | ×             |                     |
| Interparticle interactions<br>(concentrated suspensions, gels)   | ×             | ×               | ×                   | ×              |               |                     |
| Particle or pore pair distribution function<br>(concentrated suspensions, gels, fractal aggregates,<br>cements)      | ×             | ×               | ×                   | ×              |               |                     |
| Local structure and atomic pair distribution function<br>(quantum dots, nanoparticle internal crystal structures)    |               |                 |                     |                | ×             | ×                   |

Many material systems exhibit heterogeneity and disorder, regardless of whether they contain components with crystal structure or not. As reviewed by several authors (*e.g.* Fratzl, 2003; Allen, 2005), obvious examples include nanoparticle (or small-particle) dispersions in liquid, cements and concretes, clays and minerals (including oil shales), porous solids of all kinds, thermal barrier coatings, nanocomposites, precipitates in metals and alloys, and even biological structures. Some more specific examples are given in Fig. 5.8.1 that demonstrate how the heterogeneous nature of a material may comprise a size distribution of discrete pores or particles, may comprise a network structure (as is frequently the case with polymers), or it may be hierarchical in nature, possibly exhibiting a fractal structure of some kind. The heterogeneity is usually disordered but, if not, coherent-diffraction hallmarks will be apparent that can be treated by an extension of crystal-diffraction principles to the microstructural ordering at coarser length scales. For a general disordered material system, small-angle scattering (SAS) methods can be applied (Kostorz, 1979), and these comprise the techniques most discussed in this chapter.

### 5.8.1.3. Small-angle and wide-angle scattering tools

As with all diffraction-based scattering techniques, the scattering intensity, as a function of the scattering-vector magnitude  $Q$  [where  $Q = 4\pi \sin \theta/\lambda$ ,  $\lambda$  is the wavelength of the radiation used and  $2\theta$  is the scattering angle], is related to the Fourier transform of the structure or microstructure of interest. Whereas for powder or single-crystal diffraction the scattering forms the diffraction pattern associated with the particular crystal structure being investigated, for SAS/WAS the scattering can also be associated with the Fourier transform of the atomic density distribution within the sample. In the case of a disordered material system this relates to the mean microstructure arrangement averaged over the sampling measurement volume and measurement time. Small-angle X-ray and neutron scattering (SAXS and SANS) are becoming increasingly important methods for measuring the statistically representative, volume-

weighted microstructures of disordered and heterogeneous material systems (Guinier & Fournet, 1955; Glatter & Kratky, 1982). Where possible, they should be used in conjunction with wide-angle X-ray or neutron scattering (WAXS and WANS) to provide quantitative phase information for the components of the heterogeneous system. Furthermore, total-scattering studies over an extended  $Q$  range, such as are possible at synchrotron X-ray beamlines or at pulsed neutron source facilities, can provide additional information on the local structure factor that defines any short-range order that may be present, and may also be used to determine, for example, the atomic pair distribution function inside diffracting nanocrystalline grains (Proffen *et al.*, 2003; Billinge & Levin, 2007; Keen & Goodwin, 2015). Total-scattering methods also supply information on thermal diffuse scattering from lattice vibrations. Thus, wide-angle and total-scattering methods should be used in conjunction with SAXS and SANS, and are discussed below for relevant situations, but our primary focus is on SAXS and SANS.

### 5.8.1.4. Tabulated summary of quantitative information obtainable

Table 5.8.1 summarizes the information obtainable from the techniques discussed in this chapter. While specific issues regarding the limitations and experimental uncertainties of the various techniques are discussed in the sections that follow, some general points can be made here. Most, but not all, scattering- and diffraction-based methods incorporate detectors that count events (*e.g.* scattered X-ray photons or neutrons) through associated electronic pulses of some kind. Thus, most statistical uncertainties in the measured intensities can be readily calculated and propagated through the data reduction (circular or sector-averaging of position-sensitive detector counts, blank-run-data subtraction, calibration and normalization, *etc.*). However, much of the data analysis and interpretation involves geometrical desmearing steps, separation of different scattering or diffraction phenomena, and Fourier transformations from the measured data in  $Q$ -space to structural and microstructural information in real space. Thus, it is critical that uncertainties and variation in

## 5.8. DISORDERED HETEROGENEOUS MATERIALS

the measured intensities remain sufficiently small so as not to introduce artifacts into the extracted structural information. Other sources of uncertainty in the structures and microstructures determined arise from finite resolution in  $Q$ , truncation effects due to the finite  $Q$  range considered, and the degree to which any one interpretative or model scheme is appropriate. These issues can play a particularly important role where different techniques are combined together for partially disordered material systems.

### 5.8.1.5. Different notations

The notation used in this chapter corresponds to that generally used in neutron scattering, although it is also increasingly used in X-ray scattering measurements carried out at X-ray synchrotron facilities. However, a different notation has also been associated with X-ray crystallography, especially small-angle X-ray scattering. See for example, Chapter 2.6 of *International Tables for Crystallography* Volume C (Glatter & May, 2006) and other texts (Guinier & Fournet, 1955; Glatter & Kratky, 1982). The principal difference in these earlier texts of relevance here is that  $h$  is used in place of  $Q$ , and  $\mathbf{h}$  in place of  $\mathbf{Q}$  when the direction of the scattering vector must be considered. (Note that  $q$  and  $\mathbf{q}$  are also common notations corresponding to  $Q$  and  $\mathbf{Q}$ .) As is well covered in these earlier texts and *International Tables*,  $\mathbf{h} = (2\pi/\lambda)(\mathbf{s} - \mathbf{s}_0)$ , where  $\mathbf{s}$  and  $\mathbf{s}_0$  are unit vectors in the scattered and incident directions, respectively. Nowadays it is more common to see  $\mathbf{Q}$  defined by  $\mathbf{Q} = \mathbf{k} - \mathbf{k}_0$  where  $\mathbf{k}$  and  $\mathbf{k}_0$  are the scattered and incident wave vectors (of magnitude  $2\pi/\lambda$ ).

### 5.8.2. Recommended measurement tools

All of the techniques discussed here utilize either X-rays or neutrons. We acknowledge the importance of light-scattering methods for the measurement of dilute, transparent, disordered systems at the micrometre scale. However, these techniques have limited applicability here, with the possible exception of dilute particulate suspensions, and they are well described elsewhere. Also, we acknowledge that increasingly sophisticated electron-scattering methods have become available with high-resolution transmission electron microscope (HRTEM), scanning TEM (STEM) and cryogenic sample-based (cryoEM) instrumentation. However, HRTEM, STEM or cryoEM facilities do not yet provide the  $Q$  range, signal-to-noise and intensity dynamic range capabilities required for SAS and total-scattering analysis. Nor do they provide the intensity calibration needed to determine the absolute scattering probabilities and the associated volume fractions or concentrations of scattering features. For these reasons, we confine our discussion to X-ray- and neutron-based methods. For X-rays, where X-ray photons interact with the atomic electron distribution, the scattering intensity increases as the square of the atomic number ( $Z$ ) density. For neutrons, where the main scattering contribution comes from neutron interactions with the atomic nuclei, there is generally greater *relative* sensitivity to low- $Z$  materials, but this depends on the specific elements and isotopes present. In fact, the neutron isotope effect allows scattering contrast variation studies (see Section 5.8.3.1.10) to be made by adjusting the isotope mix, for example, between  $\text{H}_2\text{O}$  and  $\text{D}_2\text{O}$ . Since the neutron has a magnetic moment, there is also a magnetic interaction with any atomic magnetic moments present, which can be exploited in magnetic scattering experiments (see Section 5.8.3.1.11).

### 5.8.2.1. Small-angle scattering using a position-sensitive detector

Fig. 5.8.2 shows the basic measurement geometry used in SAS measurements using a two-dimensional (2D) position-sensitive detector (PSD), together with typical reduced SAS data *versus*  $Q$ . A well collimated incident beam impinges on the sample, in which a small component of the beam is scattered out of the forward direction by small scattering angles,  $2\theta$ . Generally, the incident beam is monochromatic, or at least sufficiently so to be associated with a fixed wavelength,  $\lambda$ , and the optimum instrument geometry occurs when the incident and scattered angular resolutions are the same. In the case of SAXS (Guinier & Fournet, 1955; Glatter & Kratky, 1982), although the X-ray beam can be tightly collimated by the crystal optics, as much as possible of the incident and scattered flight paths need to be in vacuum or a non-scattering gas because air scattering attenuates the X-ray intensity significantly. For laboratory-based SAXS facilities, the energy,  $E$ , and  $\lambda$  are determined by the X-ray source used – usually either Cu  $K\alpha$  ( $E = 8.048$  keV,  $\lambda = 1.5418$  Å) or Mo  $K\alpha$  ( $E = 17.479$  keV,  $\lambda = 0.7107$  Å) X-rays. At X-ray beamlines at synchrotrons,  $\lambda$  can be selected over a wide range, with a resolution usually determined by the band pass of the monochromator crystal optics. Generally, for SAXS, the illuminated sample area is  $\sim 0.5$  mm but can be  $< 0.1$  mm at a synchrotron. The sample thickness depends on the material and the X-ray energy, but typically ranges from 0.01 mm (high  $Z$ , low  $E$ ) to 1 mm (low  $Z$ , high  $E$ ).

In the case of SANS, the linear relationship between neutron wavelength and neutron time-of-flight is exploited (Grillo, 2008).

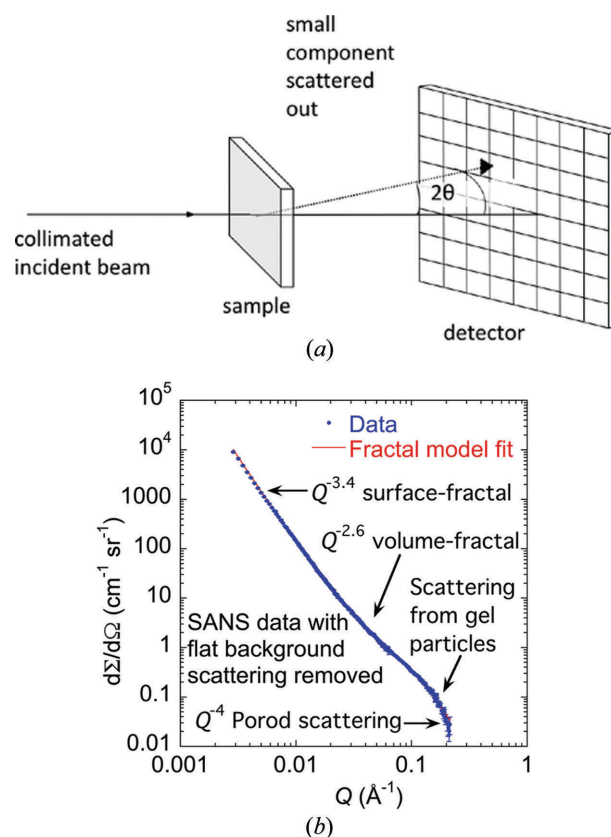


**Figure 5.8.2**

(a) Schematic of the basic measurement geometry for SAXS or SANS using a 2D PSD. The incident beam is monochromatic for SAXS and reactor-based SANS, and polychromatic for SANS at a pulsed source with energy/wavelength selection by time-of-flight. (b) Typical reduced and circularly-averaged SAS data with a fractal model fit (see Section 5.8.3.1.9). Vertical bars at each data point represent typical standard deviation uncertainties.

## 5. DEFECTS, TEXTURE AND MICROSTRUCTURE

At a reactor-based neutron facility,  $\lambda$  is determined with typically 10 to 15%  $\Delta\lambda/\lambda$  resolution about a given value using a rotating helical velocity selector (only neutrons with a velocity, hence  $\lambda$ , along the incident direction within this band pass through the rotating helical path of the velocity selector). At a spallation neutron facility all neutrons are utilized in SANS measurements with  $\lambda$  for each time bin determined from the corresponding time of flight. In SANS, unlike SAXS, neutron waveguides are frequently used to collimate the neutrons as they travel from their effective source (fission or spallation) to an effective source slit at the exit of the last guide used. This aperture subtended at the sample position largely defines the incident-beam collimation, but the incident intensity decreases with the inverse square of the distance from this last guide to the sample position. The sample aperture (*i.e.* illuminated sample area) ranges from 5 to 20 mm with sample thicknesses ranging from 0.5 to 5 mm, depending on the material.

The 2D PSD measures the scattering intensity as a function both of the scattering angle,  $2\theta$  (hence  $Q$ ), and the azimuthal angle about the incident-beam direction. Provided absolute intensity calibration is achieved (see Section 5.8.2.3) the objective in most SAXS or SANS measurements is to measure the differential scattering cross section,  $d\Sigma/d\Omega$ , as a function of  $Q$ . In this context,  $d\Sigma/d\Omega$ , for a given  $\mathbf{Q}$ , is defined as the scattering probability per unit incident flux and per unit sample volume of scattering into unit solid angle about the scattered beam direction associated with  $\mathbf{Q}$ . As in all diffraction processes,  $\mathbf{Q}$  bisects the angle between the incident-beam direction and any given scattering direction (Fig. 5.8.2a). However, for small scattering angles, we note that this puts  $\mathbf{Q}$  approximately in the sample plane. Thus, in the regular case of measurement transmission geometry, SAS primarily provides microstructural information within the sample plane, in a direction determined by the azimuthal direction of the scattering. When the microstructure within the sample is isotropic, or at least circularly symmetric about the incident-beam direction, data on the 2D PSD can be circularly averaged about the incident-beam direction and  $d\Sigma/d\Omega$  can be expressed as a function of  $Q$ , rather than  $\mathbf{Q}$ . Indeed, the most common presentation of SAS data is in a three-column format of  $Q$ ,  $d\Sigma/d\Omega$  and the standard-deviation uncertainties in  $d\Sigma/d\Omega$ , together with the necessary metadata providing the measurement geometry,  $\lambda$ ,  $Q$  resolution, sample thickness *etc.*, as well as details on the blank subtraction and the sample transmission. For SAXS or SANS with a 2D PSD, the standard-deviation uncertainties in  $d\Sigma/d\Omega$  arise primarily from statistical uncertainties in the individual pixel detector counts. However, these must be propagated through the data-reduction software as the blank subtraction, intensity calibration and azimuthal or circular averaging steps are executed.

While data reduction to give  $d\Sigma/d\Omega$  and data interpretation to model it are covered in more detail in later sections, we provide the basic theoretical basis for  $d\Sigma/d\Omega$  here. At the fundamental level (Guinier & Fournet, 1955; Glatter & Kratky, 1982; Warren, 1990)

$$\frac{d\Sigma}{d\Omega}(\mathbf{Q}) = \frac{1}{V_S} \left| \int_{V_S} \rho(\mathbf{r}) \exp(i\mathbf{Q} \cdot \mathbf{r}) d^3\mathbf{r} \right|^2, \quad (5.8.1)$$

where  $\rho(\mathbf{r})$  is the spatial distribution of the coherent X-ray or neutron scattering-length density over the sampling volume,  $V_S$ . While this equation could be applied in most diffraction-based analyses, in SAS it is more conveniently expressed in terms of the

material microstructure being studied. For an isotropic microstructure consisting of scattering particles of particle number density  $n_P$  (*i.e.*, the volume fraction  $\Phi_V = n_P V_P$ ), the squared integral in equation (5.8.1) can be converted to give a single integral in the SAS-applicable form of the Debye equation:

$$\begin{aligned} \frac{d\Sigma}{d\Omega} &= n_P |\Delta\rho|^2 V_P \int_0^\infty 4\pi r^2 \gamma_0(r) \frac{\sin(Qr)}{Qr} dr \\ &= n_P |\Delta\rho|^2 V_P^2 F_P^2(Q) S_P(Q), \end{aligned} \quad (5.8.2a)$$

where  $|\Delta\rho|^2$  is the scattering contrast factor between the particles and the surrounding medium,  $\gamma_0(r)$  is the dimensionless atomic pair correlation function,  $V_P$  is the scattering particle volume,  $F_P^2(Q)$  is the particle form factor, and  $S_P(Q)$  is an interparticle structure factor containing information on the spatial relationship between the scattering particles. Here, we initially assume that  $S_P(Q) = 1$  for a dilute population of uncorrelated particles, and we can write

$$\begin{aligned} F_P^2(Q) &= \frac{1}{V_P} \int_0^\infty 4\pi r^2 \gamma_0(r) \frac{\sin(Qr)}{Qr} dr \\ \text{where } \frac{1}{V_P} \int_0^\infty 4\pi r^2 \gamma_0(r) dr &= 1. \end{aligned} \quad (5.8.2b)$$

The particle form factor,  $F_P^2(Q)$ , can be expressed in terms of an assumed particle shape and/or real-space structure, *via*  $\gamma_0(r)$ , which decays to zero when  $r$  is greater than the maximum particle dimension, or it can be determined empirically from the data as a particle pair-distance distribution function (PDDF) (see Section 5.8.3).

Once again, we should mention a different convention frequently used in X-ray crystallography (Guinier & Fournet, 1955; Glatter & Kratky, 1982; Glatter & May, 2006). In this notation, a scattering intensity,  $I(\mathbf{h})$  is used in place of  $d\Sigma(\mathbf{Q})/d\Omega$  in equation (5.8.1) and the volume normalization is omitted. Similarly,  $I(h)$  is used in place of  $d\Sigma/d\Omega$  with the volume normalization omitted in equation (5.8.2a) *etc.* We use  $d\Sigma/d\Omega$  as it is more readily related to what is actually measured in experiments, see Section 5.8.2.3.1.

Clearly, the measurement of  $d\Sigma/d\Omega$  in a given  $Q$  regime requires sufficient  $Q$  resolution to gather the information potentially contained in the data. To cover a scale range of  $\sim 10 \text{ \AA}$  to  $\sim 0.1 \text{ mm}$ , as is typical for conventional 2D SAXS or SANS, a corresponding  $Q$  range from  $\sim 0.005$  to  $\sim 1 \text{ \AA}^{-1}$  is required, implying that several instrument configurations with different sample-to-detector distances (and corresponding incident-beam collimation) are required. In order to capture the microstructural information contained in the scattering profile, the  $Q$  resolution, defined by  $\Delta Q/Q$ , must be maintained for smaller  $Q$  values (larger scattering features). Also a correspondingly greater density of data points in  $Q$  is required if information is not to be lost. These requirements dictate tighter incident collimation and larger sample-to-detector distances for smaller  $Q$  values. However, the use of focusing optics at the more intense X-ray and neutron sources, coupled with new innovations in detector technology and the use of several 2D PSDs together, are opening up new possibilities in which SAXS or SANS data can be obtained across the whole  $Q$  range in one measurement, as discussed in Section 5.8.4.

Finally in this section, we discuss the requirements for 2D PSDs used in SAXS and SANS. Several technologies now exist

## 5.8. DISORDERED HETEROGENEOUS MATERIALS

for SAXS 2D PSDs: charge-coupled device (CCD) detectors, image plates and reverse-bias silicon-diode arrays are currently the most prominent types of X-ray 2D PSD (see Ponchut, 2006; Spieler, 2008). Several attributes need to be considered for SAXS applications: sensitive X-ray energy range, linear dynamic range in X-ray intensity, detector readout speed (this determines the cycling time, and hence time resolution of repeated measurements), spatial (pixel) resolution, signal-to-noise ratio, compactness and mass of overall detector system, and cost. All of these detector systems can be expensive, but they work well for X-ray energies up to  $\sim 12$  keV. The detector efficiency generally declines for higher energies, but can be improved by increasing the thickness of the X-ray-sensitive materials. For SAXS, CCDs are compact, have reasonable linear dynamic range in intensity (14 to 16 bits), reasonable detector readout speed (a few seconds) and good spatial resolution ( $<100$   $\mu\text{m}$  pixel size), but can have significant dark-current noise that may limit application for weak scatterers. By comparison, image plates tend to be bulky and require more extensive cooling systems, can have better linear dynamic range in intensity (up to 18 bits) and have rather long readout times ( $\sim 100$  s) that severely limit time resolution, but have excellent spatial resolution ( $\sim 10$   $\mu\text{m}$  pixel size) and low electronic backgrounds. SAXS 2D PSDs based on reverse-bias silicon-diode arrays or similar technologies currently present the best performance option (Eikenberry *et al.*, 2003).<sup>1</sup> They are light and compact, have excellent linear dynamic range in intensity (up to 20 bits), have very short detector readout speeds (a few milliseconds), acceptable spatial resolution for SAXS ( $<200$   $\mu\text{m}$  pixel size) and, as single-photon detectors, they exhibit zero dark current; but they are costly.

Development of 2D PSDs for SANS with good intensity dynamic range has progressed for several decades (Ibel, 1976; Glinka *et al.*, 1998) and continues, especially for new SANS instruments being installed at spallation neutron sources (Zhao *et al.*, 2010). Originally based on the absorption of neutrons in  $\text{BF}_3$  gas, most SANS 2D PSDs now exploit the absorption of neutrons in  $^3\text{He}$  gas (although the increasingly chronic shortage of  $^3\text{He}$  is forcing renewed consideration of  $\text{BF}_3$ ). In either case, neutron absorption results in a cascade of charged particles released in the gas close to the absorption site, and the resultant charge pulses registered on a 2D wire electrode array provide the intensity profile of the scattering intensity absorbed in the detector. The pixel resolution of SANS detectors is typically 5 to 10 mm. This is generally compatible with the larger scale of SANS instruments in general, but the detector pixel size subtended at the sample position must usually be taken into account in calculating the scattered-beam angular resolution. The dynamic intensity range of SANS 2D PSDs is more limited than for SAXS detectors ( $\sim 14$  bits). However, this limitation is partially mitigated for measurements at low  $Q$  where  $d\Sigma/d\Omega$  is larger. This is because the larger SANS sample-to-detector distance, together with the correspondingly larger required collimation distance (between the source aperture at the exit of the last collimating neutron guide and the sample), very significantly reduce the measured scattering intensity at the detector. SANS 2D PSDs are very expensive, and there is a current need to develop new technologies, both for the new generation of SANS instruments at spallation neutron sources and to address a global shortage of  $^3\text{He}$ .

<sup>1</sup> Certain commercial materials, equipment and references are identified in this paper only to specify adequately experimental procedures. In no case does such identification imply recommendation by NIST nor does it imply that the material or equipment identified is necessarily the best available for this purpose.

### 5.8.2.2. Ultra-small-angle scattering using crystal diffraction optics

In conventional SAS with a 2D PSD the  $Q$  resolution is determined by the angular resolution associated with the incident and scattered beam geometries and also, especially for SANS, by the wavelength resolution. However, SAS measurements may also be made using Bonse–Hart crystal diffraction optics (Bonse & Hart, 1966; Long *et al.*, 1991). In this case, the  $Q$  resolution is defined by the band pass and Darwin width of the crystal optics used, and the resolution is decoupled from the source or sample apertures, and from the size of the point detector used. Because the minimum  $Q$  and  $Q$  resolution are significantly finer than possible with conventional SAS, lower  $Q$  values are accessible (corresponding to coarser feature sizes), and so the Bonse–Hart method is referred to as ultra-small-angle scattering (USAXS, USAXS and USANS, corresponding to SAS, SAXS and SANS as described above).

Fig. 5.8.3(a) shows the configuration for a Bonse–Hart USAXS instrument. For both USAXS and USANS a pre-monochromated incident beam is passed through a pair of collimating crystals set to the Bragg condition for the appropriate wavelength. The X-rays or neutrons pass through the sample where small-angle scattering occurs, and then through a second pair of analysing crystals. The unscattered beam passes through both sets of crystal pairs (monoliths) when the analyser is also set to the appropriate Bragg condition. However, as the analyser is rotated away from this condition by a small angle  $2\theta$ , only X-rays or neutrons that have been scattered in the sample by the same angle satisfy the Bragg condition for the analyser monolith. Thus, a point detector placed after the analyser monolith can be used to measure the scattering intensity as a function of the analyser rotation angle,  $2\theta$ , to provide a scan of USAXS or USANS intensity *versus*  $Q$ , provided that the mechanical integrity and precision of the analyser angular rotation stage is sufficient for scanning the small angles involved. Because the  $Q$  range is scanned in a particular direction, the sample must be rotated azimuthally to obtain any anisotropic microstructural information. The fine  $Q$  resolution occurs only in the diffraction plane of the collimating and

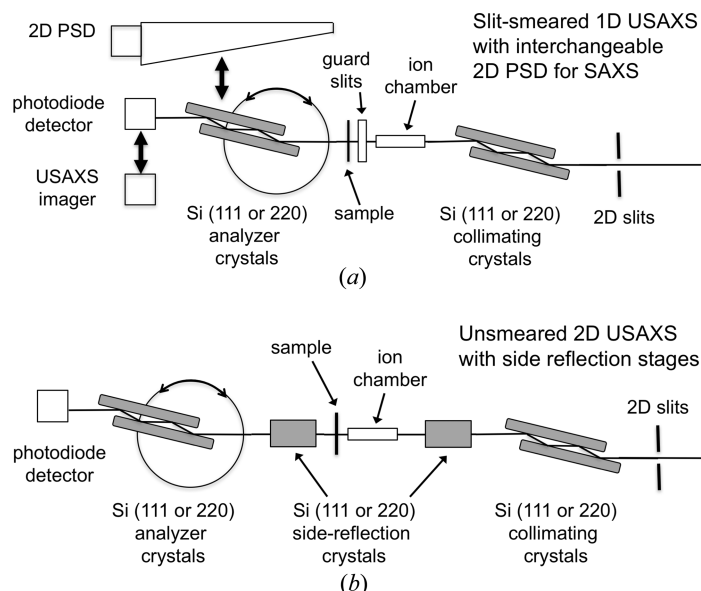


**Figure 5.8.3**

(a) Schematic of a typical USAXS instrument with regular 1D (slit-smeared) measurement configuration. (b) Schematic of a 2D (unsmear) USAXS measurement configuration. Through transverse diffractions, the side-reflection crystals remove the effects of slit smearing. Note: X-rays travel from right to left. Adapted from Ilavsky *et al.* (2009).

## 5. DEFECTS, TEXTURE AND MICROSTRUCTURE

analyser monoliths. In the transverse plane, the  $Q$  resolution is determined primarily by the angle subtended at the sample position by the detector aperture. This means that the data are intrinsically slit-smearred. While such data can be modelled directly by slit-smearing any model function, the data should be desmeared if they are to be compared with other SAS data measured with a 2D PSD. Fortunately, reliable iterative algorithms are available to accomplish this step, *e.g.* Lake (1967), *provided* that the statistical fluctuations in the data due to noise and other random uncertainties are small compared with genuine features in the scattering curve. If this is not the case, desmearing amplifies these effects, which then appear as artifacts in the desmeared data. In this situation, it is preferable to carry out slit smearing within any interpretation model being considered, and then fit this directly to the slit-smearred data without desmearing the experimental data.

Bonse–Hart USAXS and USANS instruments have developed along somewhat different lines because of the different challenges that have needed to be addressed for acceptable performance to be achieved with X-rays and neutrons. Initially, both USAXS and USANS instruments were developed simply to extend the minimum attainable  $Q$  range in SAS measurements to smaller values, and hence extend the microstructure characterization of heterogeneous systems to  $\mu\text{m}$  length scales. By combining USAS with SAS measurements it is possible to obtain statistically representative microstructure characterization over a scale range from  $10 \text{ \AA}$  to several  $\mu\text{m}$ , while wide-angle scattering and other powder-diffraction methods provide information at the  $\text{\AA}$  scale. Much of the motivation for this comes from a growing realization that processes within material systems occur across length scales with nanoscale phenomena affecting micro-scale structure and *vice versa*.

USAXS instrumentation has been developed both for laboratory-based use and at synchrotron beamlines. Typically, the collimating and analyser monoliths are set up to accommodate four crystal reflections each. This provides an overall instrumental rocking curve with a full width at half maximum, FWHM, that is approximately equal to the Darwin width for the crystal reflection used [typically Si (111) or Si (220)] and rocking-curve tails that should be much steeper than the fall-off in the USAXS intensity from any sample. In practice, USAXS measurements are extremely sensitive to the state of the crystal surfaces in both monoliths, and careful polishing and etching are required to ensure that neither strain variation nor surface roughness introduce significant artifacts into the USAXS data. Features on the crystal surfaces inevitably contribute some scattering to the instrumental ‘blank’ runs, but this is not an issue provided such contributions are much less than the genuine USAXS intensity from samples of interest. The point detector is typically a photodiode. With appropriate supporting electronics, this can have a dynamic range in X-ray intensity of more than 10 decades. Thus, at a synchrotron beamline and with precautions to reduce parasitic background effects due to air scattering *etc.*, this is sufficient to measure the intensity profile over the incident beam at  $Q = 0$ , out into the full SAXS range discussed in the previous section with 2D PSDs in a single USAXS scan. Thus USAXS instruments at a synchrotron can be used in place of SAXS with a 2D PSD, although the signal-to-noise ratio of a well-set-up conventional SAXS instrument is usually better at high  $Q$ . The typical  $Q$  range of a synchrotron-based USAXS instrument is  $0.0001$  to  $1 \text{ \AA}^{-1}$ , with the minimum  $Q$  also the  $Q$  resolution. At the lowest  $Q$  values scanned the increment in  $Q$  needs to be close to  $0.0001 \text{ \AA}^{-1}$  in order to capture all of the available micro-

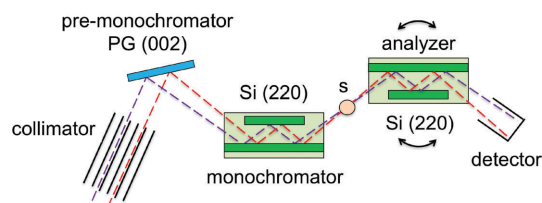


**Figure 5.8.4**

Schematic of typical USANS configuration at a reactor-based neutron source: s = sample, PG = pyrolytic graphite. Courtesy: J. Barker (NIST Center for Neutron Research).

structure information. At larger  $Q$  values, the increment can be increased logarithmically to reduce the overall scan times (Ilavsky *et al.*, 2009).

The high brilliance of third-generation X-ray synchrotrons enables USAXS instrumentation to be developed and enhanced in several ways, some of which are discussed in later sections. However, one modified mode of operation should be mentioned here. While the standard USAXS configuration provides slit-smearred data, the slit smearing can be removed by inserting two transverse crystal pairs, one after the main collimating monolith, and the other before the analyser monolith. This 2D-USAXS configuration is shown in Fig. 5.8.3(b). While the USAXS scan still occurs in a single azimuthal direction of  $Q$ , the data are now unsmearred. Full anisotropic information for a sample can now be obtained by successive USAXS scans with different azimuthal sample orientations.

USANS can extend the SAS  $Q$  range to lower minimum  $Q$  values than USAXS. This is because the Darwin width of any given crystal’s rocking curve for neutron diffraction is intrinsically narrower than for X-rays. However, for many years, the usefulness of USANS was severely limited because of low incident beam flux and the presence of high parasitic background scattering effects. One cause of the background was removed early on by having an odd number of Bragg reflections (usually three) in each crystal pair. This has the effect of removing the instrument from the direct path of parasitic (fast) neutrons coming from the source (Schwahn *et al.*, 1985). However, there remained a major parasitic background contribution, which was ultimately shown to arise from the high penetrating power of neutrons allowing multiple back reflections from the crystals in the collimating and analyser monoliths. In more recent years the problem has been solved by making cuts in the crystals and installing shielding inserts, or otherwise shielding out the contribution from crystal back reflections (Agamalian *et al.*, 1997). While the low incident neutron flux, with respect to X-rays, will probably always limit USANS to providing slit-smearred data in the low- $Q$  regime only, the use of a pyrolytic graphite (PG) pre-mono-chromator that is convergent in the transverse plane increases the effective incident flux significantly without degrading the instrument performance. With these innovations, very acceptable USANS performance can now be achieved in a  $Q$  range from  $0.00003$  to  $\sim 0.005 \text{ \AA}^{-1}$ , depending on the sample (Barker *et al.*, 2005). This is sufficient to characterize microstructural length scales up to  $\sim 30 \mu\text{m}$ , while also providing overlap with conventional SANS instruments using a 2D PSD, especially with the recent introduction of neutron lenses, discussed in Section 5.8.4. A typical USANS instrument is shown schematically in Fig. 5.8.4. As with USAXS, a point detector is used for USANS, such as a  $\text{BF}_3$  gas-filled counter. It must be well shielded against any fast neutron background, and requires sufficient intensity dynamic range to allow scans over the entire incident-beam profile.

## 5.8. DISORDERED HETEROGENEOUS MATERIALS

### 5.8.2.3. Data reduction and calibration of small-angle scattering data

For all SAS measurements made using transmission geometry, the measured data must be corrected for sample transmission (absorption and other attenuation effects) and for background scattering effects, and then the data must be absolute-calibrated to obtain  $d\Sigma/d\Omega$ . To do this requires normalizing the scattering intensity to the incident-beam intensity using some monitor detector that provides a measure of the incident-beam intensity (monitor counts) without significantly attenuating it. The monitor counts are usually measured using an ion chamber for SAXS or a fission monitor detector for SANS. X-rays or neutrons, respectively, pass through each of these types of detector with only minimal loss of beam intensity. In the absence of multiple scattering, the sample transmission,  $T_S$ , is the ratio of the scattering intensity at  $Q = 0$  when the sample is present to that at  $Q = 0$  for the empty beam (blank), and is reduced from unity by sample absorption and by all processes in the sample that attenuate the beam *including* SAS. To obtain  $T_S$  accurately, the beam intensity is integrated over a region around  $Q = 0$  to include the complete profile both of the incident beam (measured without the sample present) and of the transmitted beam measured through the sample.

#### 5.8.2.3.1. Reduction and calibration of 2D SAS data from a position-sensitive detector

For a 2D PSD, the intensity,  $I_C(i, j)$ , in pixel  $(i, j)$ , normalized to the incident beam and corrected for both electronic background and scattering background effects, is given by (Guinier & Fournet, 1955; Glatter & Kratky, 1982; Kline, 2006; Ilavsky, 2012)

$$I_C(i, j) = \left[ \frac{I_S(i, j)}{M_S} - \frac{I_{BGD}(i, j)}{M_{BGD}} \right] - T_S \left[ \frac{I_{EB}(i, j)}{M_{EB}} - \frac{I_{BGD}(i, j)}{M_{BGD}} \right], \quad (5.8.3)$$

where  $I_S(i, j)$ ,  $I_{BGD}(i, j)$  and  $I_{EB}(i, j)$  are the measured intensities for the sample, the electronic (beam off) dark current background and the empty beam runs, respectively;  $M_S$ ,  $M_{BGD}$  and  $M_{EB}$  are the corresponding monitor counts for the incident beam, and  $T_S$  is the sample transmission, as defined above. The normalized  $I_C(i, j)$  data then need to be calibrated and converted to  $d\Sigma/d\Omega$ . To do this, the position of the incident beam on the 2D PSD must be determined. This defines the PSD pixel for which  $2\theta = Q = 0$ . Using the instrument configuration geometry, the scattering angle and azimuthal angle for all other  $(i, j)$  pixels can be determined, and hence the corresponding  $\mathbf{Q}_{ij}$ . In order to complete the intensity calibration and convert the  $I_C(i, j)$  or  $I_C(\mathbf{Q}_{ij})$  to  $d\Sigma/d\Omega$ , we can apply from first principles the following relation:

$$\frac{d\Sigma}{d\Omega}(\mathbf{Q}_{ij}) = \frac{I_C(\mathbf{Q}_{ij})}{I_{EB}(0)} \left( \frac{1}{T_{SS} \tau_s \Delta\Omega} \right), \quad (5.8.4)$$

where  $I_{EB}(0)$  is the incident-beam intensity at  $Q = 0$  measured under the same conditions as for the sample,  $\tau_s$  is the sample thickness and  $\Delta\Omega$  is the solid angle subtended at the sample by one detector element. For SAS absolute intensity calibration purposes, the sample transmission,  $T_{SS}$  in equation (5.8.4), should *exclude* any incident-beam attenuation due to SAS itself. In most practical cases,  $T_{SS} \simeq T_S = I_C(0)/I_{EB}(0)$ , and the actual measured sample transmission,  $T_S$ , can be used in equation (5.8.4) in place of  $T_{SS}$ . However, if significant multiple scattering is present, the

measured  $T_S < T_{SS}$ , and a multiple-scattering correction must be made (see Section 5.8.2.3.3).

Unfortunately, for most conventional SAS measurements using a 2D PSD, the detector does not have sufficient dynamic range to measure the incident-beam intensity and frequently it must be protected by a beam stop from damage due to exposure to the full incident-beam intensity during SAS measurements. To measure  $T_S$ , attenuators are required to protect the PSD during both the sample and empty beam measurements. Nowadays, the accepted best practice is to calibrate the attenuators, and simply multiply the right-hand side of equation (5.8.4) (using the measured  $T_S$  in place of  $T_{SS}$ ) by the inverse of the calibrated attenuation factor. However, the intensity calibration can also be carried out using a calibration standard sample. A ‘primary’ calibration standard may be used, calibrated using the primary (first-principles) relation described in equation (5.8.4) at a SAS instrument where the detector can indeed withstand the full incident-beam intensity. The SAS intensity is then measured at any other instrument for both the standard and the sample(s) of interest. The intensity factor required to put the standard’s measured scattering intensity onto its known absolute scale is determined, and this same factor is then used to calibrate data from any ‘unknown’ sample. A recently established standard of this kind is the NIST Standard Reference Material SRM 3600, which is a SAXS intensity calibration standard based on glass carbon (Allen *et al.*, 2017). Alternatively, a ‘secondary’ standard can be used, such as a monodispersed silica sphere suspension of known volume concentration. The SAS data can be fitted using one of the models discussed in Section 5.8.3 such as the Guinier approximation, and the data calibrated from the fit result.

Finally, 2D PSD SAS data can be sector-averaged over an azimuthal range to give  $d\Sigma/d\Omega$  as a function of  $\mathbf{Q}$ , where the  $\mathbf{Q}$  direction is associated with the mean azimuthal angle of the sector. More usually, when the scattering is circularly symmetric about the incident-beam direction, the data are circularly averaged to give  $d\Sigma/d\Omega$  as a function of  $Q$ .

#### 5.8.2.3.2. Reduction and calibration of 1D USAXS or USANS data

For 1D USAS data, the 2D  $(i, j)$  indexing can be replaced from the outset by a 1D indexing of  $Q$  values, with the direction of  $\mathbf{Q}$  defined by the plane of the instrument’s diffraction optics and by the direction of scanning. In USAS measurements it is important that the scattering profile is measured over the centre of the rocking-curve peak in order to establish accurately where  $Q = 0$ . All other  $Q$  values are measured relative to this to give  $I_C(Q)$  after applying a 1D form of equation (5.8.3). In both USAXS and USANS instruments, the detector has sufficient intensity dynamic range to measure the incident-beam intensity directly, so that  $I_C(Q)$  can be converted to  $d\Sigma(Q)/d\Omega$  using a 1D form of equation (5.8.4). For USAS measurements,  $\Delta\Omega$  is the product of the angle subtended at the sample by the slit length in the direction transverse to the diffraction plane and the Darwin-based angular diffraction width in the diffraction plane. In the usual case of 1D USAXS or USANS, the calibrated  $d\Sigma/d\Omega$  is slit-smearred and should be desmeared as described in Section 5.8.2.2.

#### 5.8.2.3.3. Corrections for multiple scattering and flat background

A correction must be applied to the calibration when significant multiple-scattering effects are present. In the case of copious multiple SAS, there is significant broadening of the X-ray or neutron beam profile transmitted through the sample (*i.e.*, no

## 5. DEFECTS, TEXTURE AND MICROSTRUCTURE

unscattered beam survives passage through the sample). This situation is usually associated with a high concentration of strongly scattering coarse features, and a specialized analysis is required (Berk & Hardman-Rhyné, 1985, 1988). For the usual case, where the SAS remains distinguishable from the transmitted beam profile but where the total probability of small-angle scattering is greater than 5–10% of the incident beam, a more subtle correction suffices. Schelten & Schmatz (1980) developed a treatment of this situation that is still widely used at SANS facilities, but can also be applied to SAXS. In fact, any distortion of the scattering profile at low  $Q$  due to multiple scattering cannot easily be corrected. However, an intensity correction may be made that at least calibrates the intensity correctly for data at higher  $Q$  values. In this situation,  $T_S$ , measured simply from the ratio  $I_C(0)/I_{EB}(0)$ , while remaining correct for subtracting out scattering from the blank in equation (5.8.3), is significantly underestimated for use in the calibration equation (5.8.4). It should be replaced with a corrected (larger) transmission,  $T_{S\text{ corr}}$ , which is obtained by integrating  $I_C(Q)$  and  $I_{EB}(Q)$  from  $Q = 0$  out to a  $Q$  value beyond which multiple scattering is negligible for the sample being studied. The ratio of the integrals then gives  $T_{S\text{ corr}} [= T_{SS}$  in equation (5.8.4)].

Finally, many samples show flat background-scattering contributions in addition to the true SAS contribution. For X-rays, this arises from parasitic scattering contributions such as air scattering or scattering from the windows of the sample cell. For neutrons, incoherent flat background scattering results from the difference in the neutron interaction with a nuclide depending on whether the neutron and nuclear spins are parallel or anti-parallel. The average of the two cases gives rise to the coherent scattering on which SANS and ND are based. The spatially random fluctuations between the two cases leads to an incoherent flat background. For X-rays or neutrons, the flat background scattering should be subtracted out before applying the various interpretation models described in Section 5.8.3. If the flat background scattering is obvious at high  $Q$ , it can be directly subtracted out. If not, it can sometimes be determined by fitting the Porod scattering at high  $Q$  (see Section 5.8.3.1.2).

### 5.8.2.4. Reflectivity, grazing-incidence small-angle scattering and diffraction

All of the SAS methods discussed in previous sections assume transmission measurement geometry, but this precludes a major class of heterogeneous material systems of increasing technological importance: thin-film microstructures on a substrate. For such systems SAS and related measurements in reflection geometry are of interest. X-ray and neutron reflectivity (XRR and NR), where  $\mathbf{Q}$  is perpendicular to the substrate, provide depth-dependent structural information for a thin film (Parratt, 1954). Grazing-incidence SAXS and SANS (GI-SAXS and GI-SANS), and, utilizing the high penetrating power of neutrons for thicker layers and coatings, near-surface SANS (NS-SANS) can provide microstructural information both as a function of film depth and within the plane of the film (Levine *et al.*, 1991; Hamilton *et al.*, 1996). Owing to the greater penetrating power of neutrons, NR and NS-SANS are more applicable to thicker coatings or to buried interfaces than are XRR or GI-SAXS, which are more applicable to thin films. The lower penetrating power of X-rays is frequently an advantage where information is sought on disordered or ordered structures within a film without the reflectivity or scattering data being affected by contributions from the substrate. Although NR and NS-SANS can provide

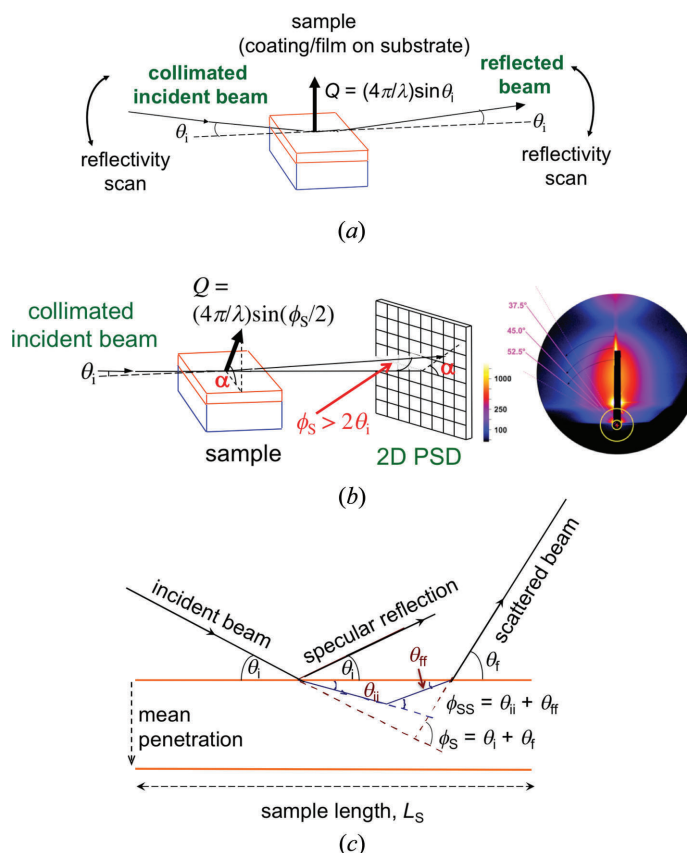


**Figure 5.8.5**

(a) Schematic of basic reflectivity measurement geometry for XRR or NR. (b) Schematic derived from Green *et al.* (2009) for GI-SAXS also showing typical 2D GI-SAXS data with sector averages. (c) Refraction and reflection geometries for GI-SAXS or NS-SANS, as discussed in the text.

important information in certain situations, thicker coatings *etc.* can usually be removed from the substrate for analysis, in section or in plane, using transmission geometry (at least with X-rays). However, thin films 10 Å to a few hundred ångströms thick (which may or may not be disordered in nature) cannot usually be removed from the substrate, and must be studied with X-rays rather than neutrons. So, in this section, we concentrate on XRR and GI-SAXS.

Fig. 5.8.5(a) shows a schematic of the basic measurement geometry for XRR or NR, while Fig. 5.8.5(b) presents a corresponding schematic for GI-SAXS or NS-SANS. For specular reflectivity the direction of  $\mathbf{Q}$  is perpendicular to the substrate plane and so information is obtained on through-thickness features, as well as effects due to surface roughness. In GI-SAXS or NS-SANS, components of  $\mathbf{Q}$  are both perpendicular to the substrate ( $\mathbf{q}_z$ ) and, depending on the azimuthal angle  $\alpha$ , parallel to the substrate ( $\mathbf{q}_y$ ). Thus, in-plane microstructure information is obtainable.

In reflectivity measurements, the intensity of the reflected beam is measured as a function of the incident angle,  $\theta_i (= \theta_r)$ . In a reflectivity scan the sample is rotated through  $\theta_i$  angles from  $0^\circ$  to the maximum  $\theta_r$  ( $\theta_{r\text{ MAX}}$ ) for which a measurable reflected beam intensity can be detected, while the detector angle,  $2\theta_r$ , is rotated from  $0^\circ$  to  $2\theta_{r\text{ MAX}}$ . In principle, the reflectivity,  $R(\theta_r)$ , can be defined as  $R(\theta_r) = I(\theta_r)/I(0)$ , where  $I(\theta_r)$  and  $I(0)$  are the measured intensities of the reflected beam for  $\theta_r$  and for  $0^\circ$ , respectively. In practice, the increasing length of the beam footprint on the sample for decreasing  $\theta_i = \theta_r$  values results in a loss of reflected intensity once the footprint is longer than the sample dimension in the reflection plane, requiring a correction to be

## 5.8. DISORDERED HETEROGENEOUS MATERIALS

made for the consequent loss in intensity actually incident on the sample. Furthermore, for a well aligned sample geometry at  $\theta_r = 0^\circ$  the sample, seen edge-on, absorbs half of the incident beam while the other half of the incident beam does not impinge on the sample at all. Thus, direct measurement of  $I(0)$  requires removal of the sample. Once corrected,  $R(\theta_r) = 1$  for  $\theta_i (= \theta_r) < \theta_C$ , where  $\theta_C$  is the critical angle for total reflection given by  $\theta_C = \lambda\{|\Delta\rho/\pi\}^{1/2}$  and  $|\Delta\rho|$  is the difference in scattering-length density across the reflecting interface. Corrected reflectivity data for  $R(\theta_r)$  versus  $\theta_r$  over sufficient angular range, and with sufficient angular resolution, must be obtained to capture the structural information associated with the thin-film layer(s). For practical purposes, laboratory-based X-ray sources can provide the required dynamic range in  $R(\theta_r)$  for XRR measurements of films thicker than  $\sim 100$  Å. For thinner films, measurements at least at a first-generation synchrotron are required, and it is usually necessary to determine the reflectivity curve from the surface of the bare substrate in order to correct for any substrate artifacts not associated with the thin-film structure of interest. Frequently, it is convenient to convert the  $\theta_r$  values to  $Q [= (4\pi/\lambda) \sin \theta_r]$  and do further analysis on corrected data for  $R(Q)$  versus  $Q$ , together with uncertainties in  $R(Q)$ .

In GI-SAXS or NS-SANS measurements the sample is oriented at a fixed grazing incident angle,  $\theta_i$ , to the incident-beam direction ( $\theta_i > \theta_C$  for scattering from within the film) and the data are collected using a 2D PSD as for conventional transmission geometry SAXS or SANS. Measurements can be made using different values of  $\theta_i$ , and the different 2D scattering data analysed to determine how the film microstructure changes with depth. By reducing  $\theta_i$  below  $\theta_C$ , it can be established whether the microstructure that causes the scattering is within the film or is located on the surface. The location where the incident beam impinges on the sample (required for calculating where  $Q = 0$  on the 2D detector), as well as the parasitic scattering contribution, can only be determined by moving the sample out of the beam. With the sample in place, both the incident beam and scattering that would be in the sample shadow as viewed from the 2D detector are occluded and unobservable. Also, the specularly reflected incident beam further obscures the data at low  $Q$ , and effectively increases the minimum observable  $Q$ . Refraction corrections must be applied to both the incident and scattered X-ray or neutron beam directions, and normalization to obtain  $d\Sigma/d\Omega$  is complicated both by the complex effective sampling volume and the need to apply the distorted-wave Born approximation (DWBA) in the data reduction and analysis when multiple reflection and scattering contributions exist (Sinha *et al.*, 1988).

For a thick film of refractive index  $n$ , given by  $n^2 = 1 - \theta_C^2$ , Fig. 5.8.5(c) illustrates the situation for scattering in the refraction plane. For an external grazing-incidence angle  $\theta_i$ , an external scattered grazing angle  $\theta_f$  and apparent scattering angle  $\varphi_S (= \theta_i + \theta_f)$ , measured outside the film, the corresponding angles inside the film are  $\theta_{ii}$ ,  $\theta_{ff}$  and  $\varphi_{SS} (= \theta_{ii} + \theta_{ff})$ , where  $\theta_{ii}^2 = \theta_i^2 - \theta_C^2$  and  $\theta_{ff}^2 = \theta_f^2 - \theta_C^2$ . For a finite azimuthal angle  $\alpha$ , the outgoing scattered grazing angles are reduced to  $\theta_2$  and  $\theta_{22}$  where  $\theta_2 = \theta_f \cos \alpha$  and  $\theta_{22}^2 = \theta_2^2 - \theta_C^2$ . Refraction effects cause corresponding changes in the components of  $\mathbf{Q}$ . While the component parallel to the substrate,  $q_p$ , is the same inside or outside the film, *i.e.*  $q'_p = q_p$ , the component normal to the film,  $q_N$ , is changed by the refraction at the film boundary, so that inside the film  $q'_N = q_N[\cos \theta_i(\sin \theta_{ii} + \sin \theta_{22})]/[\cos \theta_{ii}(\sin \theta_i + \sin \theta_2)]$  and  $Q'$  inside the film is given by  $Q'^2 = Q^2 - q_N^2 + q_N'^2$ , where  $Q$  is the apparent external value. The refraction causes all terms in the SAS

expressions to change and for a thick film (where reflection from the film/substrate interface can be ignored) it can be shown that inside the film

$$\frac{d\Sigma'}{d\Omega'}(Q') = [\cot \theta_{ii} + \cot \theta_{22}] \left( \frac{\sin \theta_{22}}{\sin \theta_2} \right) \left( \frac{1}{T_S \sin \theta_{ii}} \right) \times \left[ \frac{(\sin \theta_i + n \sin \theta_{ii})^2}{\sin \theta_i} \right]^2 \frac{d\Sigma}{d\Omega}(Q), \quad (5.8.5)$$

where  $T_S = 2[\exp(-\Sigma_T L_S) + \Sigma_T L_S - 1]/(\Sigma_T L_S)^2$  is the theoretical transmission of the sample film of length  $L_S$  along the beam direction and it is assumed that the film material has a total attenuation cross section of  $\Sigma_T$ . The value of  $\Sigma_T$  determines whether a film of thickness  $\tau_{\text{film}}$  can be considered thick or whether it must be treated as a thin film with the full DWBA formalism applied. The maximum penetration depth,  $\zeta_{\text{max}}$ , measurable for a given scattering geometry is given by  $\zeta_{\text{max}} = L_S[\cot \theta_{ii} + \cot \theta_{22}]$ . However, the mean penetration depth  $\zeta_{\text{mean}} = \zeta_{\text{max}}(1/\Sigma_T L_S)[2 + \Sigma_T L_S - (2/T_S)]$ . While generally  $\zeta_{\text{mean}} \ll \zeta_{\text{max}}$ , the criterion for a thick film is that  $\zeta_{\text{mean}} \ll \tau_{\text{film}}$ .

### 5.8.2.5. Wide-angle scattering and other methods for disordered structures

As mentioned in Section 5.8.1, a heterogeneous material system may contain crystalline components even if the heterogeneous arrangement of those components is itself disordered. For the SAS and reflectivity measurements discussed in Section 5.8.2.4, a fully quantitative analysis is only possible if the elemental composition and density of each of the components are known. This information is required in order to determine accurately the  $|\Delta\rho|^2$  contrast-factor term in equation (5.8.2a). Thus, wide-angle and powder-diffraction measurements that enable any component crystalline phases to be identified can play a critical role. General powder-diffraction characterization is covered elsewhere in this volume. However, when *in situ* studies of a disordered material undergoing some change in real time are of interest, the use of WAXS and WANS to monitor specific diffraction peaks associated with crystalline phases that may be present, even if only transitory in nature, can provide key information. Several combined SAXS/WAXS instruments have been developed at third-generation X-ray synchrotron-radiation sources to enable the simultaneous study of microstructure evolution and the appearance or disappearance of crystalline phases within the microstructure (Lai *et al.*, 2006).

Finally, some attention must be given to total-scattering methods that have evolved in recent years to interrogate the short-range or limited-range crystalline structure that can be encountered in disordered materials. These have evolved from earlier 'liquids amorphous' methods (mainly neutron-based) to quantify structure in materials with little or no crystalline structure, such as glasses (Price, 1999). However, these methods now extend to a wide range of nanocrystalline or poorly crystalline materials. The basis of such measurements is to collect contiguous data over a very large  $Q$  range with sufficient resolution and intensity throughout the  $Q$  range to quantify the degree and scale range of structure present. These requirements tend to confine such instruments to third-generation X-ray synchrotrons and pulsed-neutron-source facilities that can accommodate long beamlines. However, these instruments are now making significant progress in interrogating the whole range of disordered materials at the structural level (Billinge & Levin, 2007; see also Chapter 5.7).

## 5. DEFECTS, TEXTURE AND MICROSTRUCTURE

For powder-diffraction studies, the coherent diffraction intensity,  $I_{\text{coh}}$ , from an ensemble of  $N$  atoms is given by (Warren, 1990; Farrow & Billinge, 2009)

$$I_{\text{coh}} = \sum_{i,j} b_j^* b_i \exp(i\mathbf{Q} \cdot \mathbf{r}_{ij}) = N\langle b^2 \rangle + \sum_{i \neq j} b_j^* b_i \exp(i\mathbf{Q} \cdot \mathbf{r}_{ij}), \quad (5.8.6)$$

where  $b_i$  and  $b_j$  are the neutron scattering lengths or X-ray form factors per atom at sites  $i$  and  $j$ , respectively,  $\mathbf{r}_{ij} = \mathbf{r}_i - \mathbf{r}_j$ ,  $b^*$  denotes a complex conjugate as a function of  $\mathbf{Q}$ , and  $\langle b^2 \rangle$  is the mean-square value of  $b_i$  or  $b_j$ . The total-scattering structure factor per atom,  $S(\mathbf{Q})$ , describes the scattering between the atoms in an ensemble, and is given by

$$S(\mathbf{Q}) = 1 + \frac{\sum_{i \neq j} b_j^* b_i \exp(i\mathbf{Q} \cdot \mathbf{r}_{ij})}{N\langle b^2 \rangle}, \quad (5.8.7)$$

where  $S(\mathbf{Q}) = 1$  for isolated atoms. We note that, for neutrons,  $b_i$  and  $b_j$  are isotropic and independent of  $Q$  for scattering from the nucleus. For X-ray scattering or magnetic neutron scattering from the atomic electron distribution a correction is required at high  $Q$  because of the finite size of the atom, but this can be neglected at least for the forward scattering. Thus, for an isotropic microstructure, the Debye relation that the orientational average of  $\exp(i\mathbf{Q} \cdot \mathbf{r}_{ij})$  is equal to  $\sin(Qr_{ij})/Qr_{ij}$  can be used to give

$$S(Q) - 1 = \left( \frac{1}{N\langle b^2 \rangle} \right) \sum_{i \neq j} b_j^* b_i \left[ \frac{\sin(Qr_{ij})}{Qr_{ij}} \right]. \quad (5.8.8)$$

The  $Q$  dependence can be removed from everything except for the sine term by using the reduced total-scattering structure factor,  $S_{\text{RT}}(Q)$ , where

$$S_{\text{RT}}(Q) = Q[S(Q) - 1] = \left( \frac{1}{N\langle b^2 \rangle} \right) \sum_{i \neq j} b_j^* b_i \left[ \frac{\sin(Qr_{ij})}{r_{ij}} \right]. \quad (5.8.9)$$

The sine Fourier transform of  $S_{\text{RT}}(Q)$  gives the real-space function  $G(r)$ , where

$$G(r) = (2/\pi) \int_0^\infty S_{\text{RT}}(Q) \sin(Qr) dQ, \quad (5.8.10)$$

and by substituting equation (5.8.10) into equation (5.8.9), we get (for positive  $r$ )

$$G(r) = \left( \frac{1}{rN\langle b^2 \rangle} \right) \sum_{i \neq j} b_j^* b_i \delta(r - r_{ij}), \quad (5.8.11)$$

where  $\delta(x)$  denotes a Dirac delta function. It is clear that  $G(r)$  is a pair density distribution function, as can be shown by considering the case of an ensemble of  $N$  identical atoms:

$$\int_a^b G(r)r dr = N_{ab} = \int_a^b 4\pi r^2 n(r) dr, \quad (5.8.12)$$

where  $N_{ab}$  is the number of atoms found between a radius  $r = a$  and a radius  $r = b$ , measured from any one atom, and  $n(r)$  is the atomic number density distribution measured similarly as a function of  $r$ , thus allowing a radial distribution function,  $Y(r)$ , to be defined by  $Y(r) = 4\pi r^2 n(r)$ .

Algorithms now exist to extract  $G(r)$  versus  $r$  from measured  $I_{\text{coh}}$  data versus  $Q$ , via the derived  $[S(Q) - 1]$  and  $S_{\text{RT}}(Q)$  functions (Juhás *et al.*, 2013). Fig. 5.8.6 shows both typical total-scattering  $[S(Q) - 1]$  (model) data versus  $Q$  and the derived atomic pair distribution function,  $G(r)$  versus  $r$ . In practice, the inverse Fourier sine transform of equation (5.8.10) has finite  $Q$

limits. In particular, there is always a finite minimum  $Q$  for which the scattering and hence  $S(Q)$  can be measured. Loss of the non-measurable scattering contribution near  $Q = 0$  leads to a subtraction from the calculated pair distribution function,  $G(r)$ , that can be associated with the scattering from structure at large  $r$ . In the case of a uniform bulk material microstructure, including many glasses, the subtracted component is simply related to the averaged atomic scattering-length density,  $n_0$ , applicable over large distances, and it can be shown that (Cargill, 1971; Farrow & Billinge, 2009)

$$G(r) = 4\pi r[n(r) - n_0]. \quad (5.8.13)$$

Disordered structures can be evaluated using equations (5.8.6)–(5.8.13) in the case of bulk materials. However, when the disordered elements themselves comprise an ensemble of nanocrystalline features, the  $-4\pi n_0$  term becomes more complex; this situation is discussed further in the next section.

Meanwhile, noise in the WAXS data at high  $Q$  can cause oscillatory artifacts to appear in the  $G(r)$  function because of data truncation at a finite maximum  $Q$ . These can be removed by smoothing the data, but this still results in some loss of information in the extracted  $G(r)$  function if the level of smoothing required either significantly exceeds that due to finite instrument resolution in  $Q$ , or it reduces peak intensities significantly more

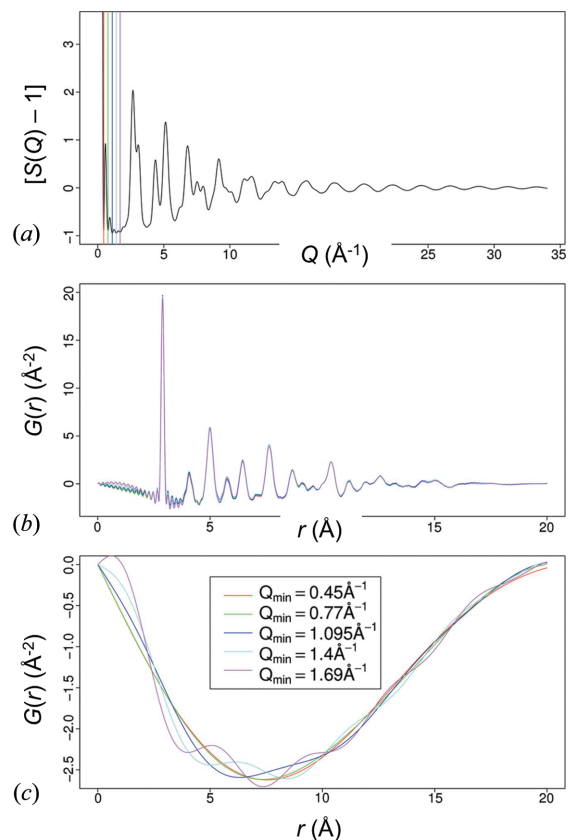


**Figure 5.8.6**

(a) Schematic of typical total-scattering  $[S(Q) - 1]$  data versus  $Q$  for model Au core-shell nanoparticles. Choices of partition between small- and wide-angle scattering are marked by vertical lines. (b) The corresponding atomic pair density distribution function,  $G(r)$ , versus  $r$ , obtained via Fourier transform of wide-angle scattering data only, starting from various minimum  $Q$  values ( $Q_{\text{min}}$ ). (c) The Fourier transform of data in the SAS range from  $Q = 0$  to  $Q = Q_{\text{min}}$  for various  $Q_{\text{min}}$ . The  $-4\pi n_0$  term of equation (5.8.13) arising from the non-measurable scattering at  $Q = 0$  is visible at low  $Q$ , but the rest of the function is related to  $\gamma_0(r)$  described in Section 5.8.3.2 for nanoparticle scattering. Adapted from Mullen & Levin (2011).

## 5.8. DISORDERED HETEROGENEOUS MATERIALS

than the Debye–Waller effect (see Section 5.8.3.3) of thermal diffuse scattering (Toby & Egami, 1992).

### 5.8.3. Quantitative analysis of disordered heterogeneous materials

In Section 5.8.2 we have set out the main experimental measurement techniques, the kind of data obtainable and how the data should be reduced to provide information on the sample material system of interest. In this section we consider how such data should be interpreted to quantify actual structural and microstructural parameters of interest for disordered material systems. It is not possible to cover every interpretative scheme in existence, but the main classes of interpretative schemes and models are reviewed to give a sense of the range of analyses possible.

#### 5.8.3.1. Interpretative models for analysis of SAS data

##### 5.8.3.1.1. Guinier approximation

Assuming any flat background scattering has been subtracted, the heterogeneous system is sufficiently disordered and dilute that the structure-factor term,  $S(Q)$ , in equation (5.8.2a) can be assumed to be unity and the inhomogeneities are approximately monodispersed in size and shape, perhaps the simplest interpretative approximation for SAS data is the Guinier approximation (Guinier & Fournet, 1955):

$$\frac{d\Sigma}{d\Omega} = \Phi_V |\Delta\rho|^2 V_P \exp\left(-\frac{Q^2 R_G^2}{3}\right), \quad QR_G < \sim 1, \quad (5.8.14)$$

where  $R_G$  is the Guinier radius (mean radius of gyration) of the scattering features. For spherical particles or voids of radius  $R_P$ ,  $R_G^2 = 3R_P^2/5$  and  $V_P = 4\pi R_P^3/3$ . While the approximation is only valid for  $QR_G < \sim 1$ , equation (5.8.14) clearly shows how the width of the scattering profile is inversely related to the size of the scattering features. We also note that the SAS intensity is proportional both to the volume fraction of scattering features present and to their individual mean volumes. Thus, SAS methods will be strongly volume-weighted over any size distribution of inhomogeneities that may actually be present.

##### 5.8.3.1.2. Porod scattering regime

At high  $Q$  values the SAS intensity can be related to the specific surface area of the scattering features (Porod, 1951, 1952):

$$\frac{d\Sigma}{d\Omega} = \frac{2\pi |\Delta\rho|^2 S_V}{Q^4} + \text{BGD}, \quad QR_G \gg 1, \quad (5.8.15)$$

where  $S_V$  is the surface area per unit sample volume and BGD is any residual flat background scattering that needs to be considered at high  $Q$  where the true SAS scattering intensity is weak. Frequently, it is convenient to plot  $Q^4 d\Sigma/d\Omega$  versus  $Q^4$  for high  $Q$  and fit a straight-line slope of gradient BGD and intercept  $2\pi |\Delta\rho|^2 S_V$ . (Note that this provides a means of determining the flat background, BGD.) Thus, just as equation (5.8.14) provides information on the volume fraction of the inhomogeneities in a disordered system, equation (5.8.15) provides the corresponding surface-area information – provided that the contrast factor,  $|\Delta\rho|^2$ , is known. Even when  $|\Delta\rho|^2$  is not known, the ratio of the two front terms of these equations provides the surface area per

unit volume of the individual inhomogeneities themselves, because  $|\Delta\rho|^2$  cancels out.

##### 5.8.3.1.3. Scattering invariant

The volume fraction of the inhomogeneous features giving rise to SAXS or SANS can be more generally related to the overall scattering through the so-called scattering invariant (Glatter & Kratky, 1982), which is essentially the SAS intensity integrated over all  $Q$ :

$$2\pi^2 \Phi_V (1 - \Phi_V) |\Delta\rho|^2 = \int_0^\infty Q^2 \frac{d\Sigma}{d\Omega}(Q) dQ, \quad (5.8.16)$$

where the integral is taken over all  $Q$  values (equivalent to scattering over a  $4\pi$  solid angle). In principle, if  $|\Delta\rho|^2$  is known, the volume fraction of the scattering features,  $\Phi_V$ , can be determined independently of the specific morphology or disordered arrangement. Experimentally, the integrand on the right-hand side of equation (5.8.16) must usually be extrapolated beyond the measured  $Q$  range, both at low  $Q$  and at high  $Q$  where the  $Q^2$ -weighted SAS intensity is weak and a careful flat background subtraction must be made.

##### 5.8.3.1.4. Debye–Bueche model

While many disordered material systems contain discrete particles or pores that comprise the inhomogeneities giving rise to SAS, this is not necessarily the case. For example, polymer blends may contain separate (non-mixing) phases separated by an interface that permeates throughout the sampling volume. Assuming the two phases (1 and 2) permeate the sampling volume randomly with a characteristic (Debye) length  $\xi$ , then it can be shown that the scattering is given by (Debye & Bueche, 1949)

$$\frac{d\Sigma}{d\Omega} = \frac{8\pi\xi^3 \Phi_{1V} \Phi_{2V} |\Delta\rho|^2}{(1 + Q^2\xi^2)^2}, \quad (5.8.17)$$

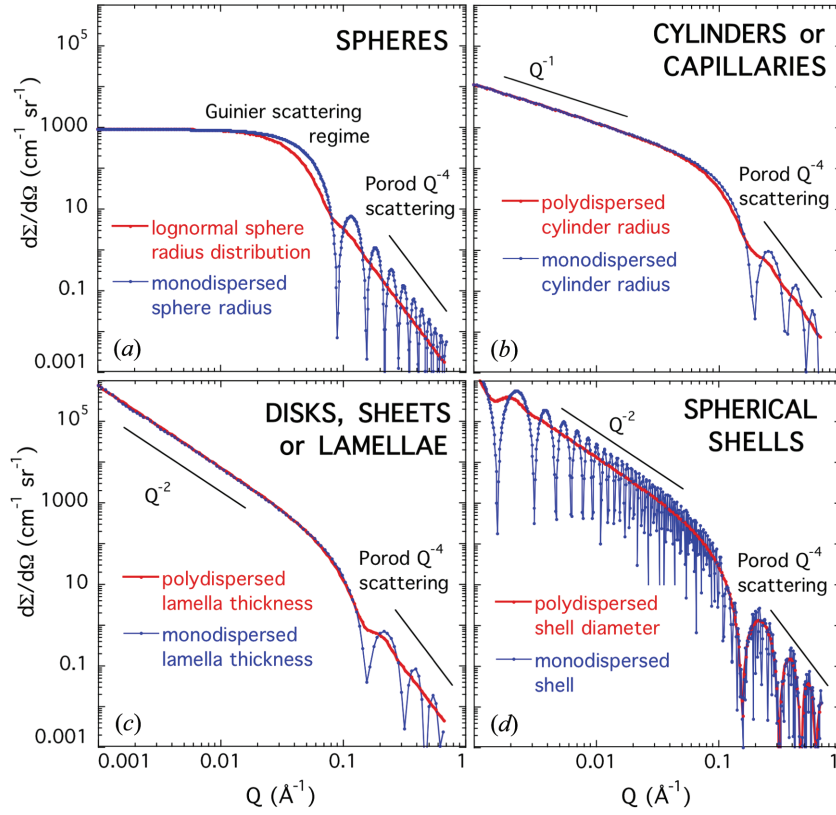
where  $\Phi_{1V}$  and  $\Phi_{2V}$  are the volume fractions of the two phases ( $\Phi_{1V} + \Phi_{2V} = 1$ ) and  $|\Delta\rho|^2$  is the scattering contrast factor between phases 1 and 2. Assuming that  $|\Delta\rho|^2$  is known, a Lorentzian function can be fitted to obtain  $\xi$  from the intensity variation in  $Q$ , then  $\Phi_{1V}$  and  $\Phi_{2V}$  determined from the absolute scattering intensity, together with the constraint that they must sum to unity. We also note that, in the limit of high  $Q$ , equation (5.8.17) gives Porod  $Q^{-4}$  scattering, and the surface area,  $S_v$ , so obtained can be related to the variables  $\Phi_{1V}$ ,  $\Phi_{2V}$  and  $\xi$  determined by  $S_v = 4\Phi_{1V}\Phi_{2V}/\xi$ .

##### 5.8.3.1.5. Shape effects in the form factor

As we have indicated, equations (5.8.14) and (5.8.15) provide working approximations for the scattering intensity at low  $Q$  and at high  $Q$  for a dilute population of randomly oriented scattering features. However, analytical expressions have been established for the scattering intensity at all  $Q$  for dilute populations of randomly oriented scattering features of specific shape that are also monodispersed in size and shape. For example, see Pedersen (1997). Here we summarize a few of the more significant generic expressions for  $d\Sigma/d\Omega$  associated with scattering features of specific shape (also see Fig. 5.8.7):

- (i) *Spheroidal features of orthogonal radii*  $R_O$ ,  $R_O$ ,  $\beta R_O$  (Shull & Roess, 1947; Roess & Shull, 1947):

## 5. DEFECTS, TEXTURE AND MICROSTRUCTURE


**Figure 5.8.7**

Characteristic SAS intensity profiles of ensembles of scattering features, both monodispersed and polydispersed in size. (a) Spheres of mean diameter 100 Å; (b) cylinders or capillaries of mean diameter 40 Å and length 4000 Å; (c) discs or lamellae of mean thickness 40 Å and diameter 4000 Å; and (d) spherical shells of mean diameter 4000 Å and fixed shell thickness 40 Å. Porod scattering and other characteristic power laws are indicated. Note that 20% polydispersity in size is sufficient to eliminate much of the Bessel-function oscillation found in the scattering from monodispersed features. Functions are derived using software developed by S. R. Kline of NIST Center for Neutron Research (Kline, 2006).

$$\frac{d\Sigma}{d\Omega} = \Phi_V |\Delta\rho|^2 V_p \frac{9\pi}{2} \int_0^1 \frac{[J_{3/2}(u)]^2}{u^3} dX, \quad (5.8.18)$$

where  $V_p = 4\pi\beta R_o^3/3$ , the ordinary Bessel function  $J_{3/2}(u) = (2/\pi)^{1/2}(\sin u - u \cos u)/u^{3/2}$ ,  $u = QR_o K(\beta, X)$ ,  $K(\beta, X) = [1 + (\beta^2 - 1)X^2]^{1/2}$ ,  $X = \cos \eta$ , and  $\eta$  is the angle between the direction of  $\mathbf{Q}$  and the  $\beta R_o$  axis of the spheroid. In the case of  $\beta = 1$  we get for spherical features

$$\frac{d\Sigma}{d\Omega} = \Phi_V |\Delta\rho|^2 V_p \left[ 3 \left( \frac{\sin(QR_o) - QR_o \cos(QR_o)}{(QR_o)^3} \right) \right]^2. \quad (5.8.19)$$

The average intensity of the Bessel function oscillations in equations (5.8.18) and (5.8.19) can be approximated as a function of  $Q$ : in the small- $Q$  regime by equation (5.8.14) where  $R_G^2 = (2 + \beta^2)R_o^2/5$ , and in the large- $Q$  regime by equation (5.8.15) where, for a spheroid,

$$S_V = \frac{3\Phi_V \chi_S}{R_o} \quad (5.8.20a)$$

$$\chi_S = \frac{1}{2\beta} \left\{ 1 + \frac{\beta^2}{(1 - \beta^2)^{1/2}} \ln \left[ \frac{1 + (1 - \beta^2)^{1/2}}{\beta} \right] \right\} \quad \beta \leq 1, \quad (5.8.20b)$$

$$\chi_S = \frac{1}{2\beta} \left\{ 1 + \frac{\beta^2}{(\beta^2 - 1)^{1/2}} \arcsin \left[ \frac{(\beta^2 - 1)^{1/2}}{\beta} \right] \right\} \quad \beta \geq 1, \quad (5.8.20c)$$

and we note that  $\chi_S = 1$  for  $\beta = 1$ .

(ii) *Discs, sheets or laminar pores of diameter  $2R_D$  and thickness  $\tau_D$ , where  $\tau_D \ll 2R_D$  (Guinier & Fournet, 1955; Glatter & Kratky, 1982). Again, assuming a dilute ensemble of randomly oriented scattering features, it can be shown that*

$$\frac{d\Sigma}{d\Omega} = \Phi_V |\Delta\rho|^2 V_p \int_0^1 \left| 2J_0 \left( \frac{Q\tau_D X}{2} \right) \frac{J_1 \left[ QR_D(1 - X^2)^{1/2} \right]}{QR_D(1 - X^2)^{1/2}} \right|^2 dX, \quad (5.8.21a)$$

where  $X = \cos \eta$  and  $\eta$  is the angle between the axis of the disc and the direction of  $\mathbf{Q}$ , here  $V_p = \pi R_D^2 \tau_D$ , and the spherical Bessel functions are given by  $J_0(u) = \sin u/u$  and  $J_1(v) = (\sin v - v \cos v)/v^2$ . Equation (5.8.21a) is in fact valid for all values of  $\tau_D$  and  $R_D$ , but for  $\tau_D \ll 2R_D$  and neglecting the Bessel-function oscillations, the scattering intensity follows a  $Q^{-2}$  power law in the regime  $R_D^{-1} \ll Q \ll 2\tau_D^{-1}$  and a  $Q^{-4}$  Porod power law for  $Q \gg 2\tau_D^{-1}$ . For near-infinitesimal  $\tau_D$ ,  $d\Sigma/d\Omega$  is given by

$$\frac{d\Sigma}{d\Omega} = \Phi_V |\Delta\rho|^2 V_p \left[ 1 - \frac{J_1(2QR_D)}{QR_D} \right] \frac{2}{(QR_D)^2}, \quad (5.8.21b)$$

where the spherical Bessel function  $J_1(v) = (\sin v - v \cos v)/v^2$  and there is no Porod  $Q^{-4}$  scattering. The terminal slope  $\simeq Q^{-2}$  for  $Q \gg R_D^{-1}$ . There is, however, a Guinier regime at low  $Q$  with  $R_G^2 = R_D^2/2$ .

(iii) *Cylinders, rods or capillary pores of radius  $r_C$  and length  $L$ , where  $L \gg 2r_C$  (Guinier & Fournet, 1955; Glatter & Kratky, 1982):*

## 5.8. DISORDERED HETEROGENEOUS MATERIALS

$$\frac{d\Sigma}{d\Omega} = \Phi_V |\Delta\rho|^2 V_P \int_0^1 \left| 2J_0\left(\frac{QLX}{2}\right) \frac{J_1\left[Qr_c(1-X^2)^{1/2}\right]}{Qr_c(1-X^2)^{1/2}} \right|^2 dX, \quad (5.8.21c)$$

where  $X = \cos \eta$  and  $\eta$  is the angle between the axis of the cylinder and the direction of  $\mathbf{Q}$ ; here  $V_P = \pi r_c^2 L$ , and the spherical Bessel functions are given by  $J_0(u) = \sin u/u$  and  $J_1(v) = (\sin v - v \cos v)/v^2$ . Again, equation (5.8.21c) is valid for all  $r_c$  and  $L$ , and is in fact mathematically identical to equation (5.8.21a). However, for  $L \gg 2r_c$  and neglecting the Bessel-function oscillations, the scattering intensity follows a  $Q^{-1}$  power law in the regime  $2L^{-1} \ll Q \ll r_c^{-1}$  and a  $Q^{-4}$  Porod power law for  $Q \gg r_c^{-1}$ . For near-infinitesimal  $r_c$ ,  $d\Sigma/d\Omega$  is given by

$$\frac{d\Sigma}{d\Omega} = \Phi_V |\Delta\rho|^2 V_P \left[ \frac{2S_i(QL)}{QL} - \frac{\sin^2(QL/2)}{(QL/2)^2} \right], \quad (5.8.21d)$$

where  $S_i(QL) = \int_0^{QL} (\sin u/u) du$ . In this case, there is again no Porod  $Q^{-4}$  scattering and the terminal slope  $\simeq Q^{-1}$  for  $Q \gg 2L^{-1}$ , but there is a Guinier regime at low  $Q$  with  $R_G^2 = L^2/12$ .

- (iv) *Gaussian coil morphology (common in polymer science)* (Debye, 1947). SAS (especially SANS) has been applied to a myriad of situations in polymer science. It is not possible here to include all of the form factors of interest, and these have been reviewed elsewhere (Pedersen, 2000). Nevertheless, we include one generic case, common in polymer science, which is that of a polymer Gaussian coil with mean radius of gyration  $R_G$  and mean volume  $V_P$ :

$$\frac{d\Sigma}{d\Omega} = \Phi_V |\Delta\rho|^2 V_P \left\{ 2 \frac{[\exp(-Q^2 R_G^2) + Q^2 R_G^2 - 1]}{Q^4 R_G^4} \right\}. \quad (5.8.22)$$

In many practical polymer applications, it is convenient to re-write  $\Phi_V$  and  $V_P$  in terms of the polymer molecular mass and density. It should be noted that for  $QR_G \gg 1$ , equation (5.8.22) predicts that  $d\Sigma/d\Omega \simeq Q^{-2}$ , similar to the power law found for the scattering from thin discs.

- (v) *Core-shell particles* (Guinier & Fournet, 1955). Many SAS applications involve core-shell particles of one kind or another. These range from quantum-dot nanoparticles involving more than one component, through many systems where the scattering particles are coated with other organic or inorganic species, to the entire class of hollow particles (including micelles and vesicles). It is not feasible to cover all core-shell particle types here, but a generic example is given for guidance. Essentially, the SAS intensity for a core-shell particle is determined by considering it as an inner particle inside an outer particle. The form factor of the inner particle core with respect to the shell is summed coherently with the form factor of the outer particle with respect to the external medium. For a spherical core-shell particle of overall (shell) radius,  $R_{\text{shell}}$  and internal (core) radius,  $R_{\text{core}}$ , with X-ray or neutron scattering-length densities  $\rho_{\text{shell}}$ ,  $\rho_{\text{core}}$  and  $\rho_o$ , respectively, for the shell, core and external (solvent) medium

$$\begin{aligned} \frac{d\Sigma}{d\Omega} = & \frac{\Phi_V}{V_P} \left\{ \left[ 3V_C(\rho_{\text{core}} - \rho_{\text{shell}}) \frac{[\sin(QR_{\text{core}}) - QR_{\text{core}} \cos(QR_{\text{core}})]}{(QR_{\text{core}})^3} \right] \right. \\ & \left. + \left[ 3V_P(\rho_{\text{shell}} - \rho_o) \frac{[\sin(QR_{\text{shell}}) - QR_{\text{shell}} \cos(QR_{\text{shell}})]}{(QR_{\text{shell}})^3} \right] \right\}^2, \end{aligned} \quad (5.8.23)$$

where  $\Phi_V$  is the volume fraction of the overall particles of volume  $V_P = 4\pi R_{\text{shell}}^3/3$ , and  $V_C = 4\pi R_{\text{core}}^3/3$ . Equation (5.8.23) can be re-written in terms of the core volume and core volume fraction, or the shell volume and shell volume fraction, by re-scaling  $\Phi_V$  and  $V_P$  appropriately. While the equations become more complex, the same basic principle applies to the scattering intensity from other core-shell particle shapes. For a hollow particle where  $\rho_{\text{core}} = \rho_o$ , the inner particle is essentially subtracted from the outer particle in the form-factor term before squaring. In such a case where the shell thickness  $\tau_{\text{shell}} \ll R_{\text{core}}$  (and  $R_{\text{shell}}$ ), equation (5.8.23) gives  $Q^{-2}$  scattering in the regime  $R_{\text{core}}^{-1} \ll Q \ll \tau_{\text{shell}}^{-1}$ . Note that this is the third scenario discussed in this section where  $Q^{-2}$  scattering is observed. Prior knowledge is needed in such scenarios to determine which one applies.

The characteristic SAS intensity as a function of  $Q$  is illustrated for several of the above scenarios in Fig. 5.8.7. The scattering from randomly oriented, monodispersed scattering features is compared with that from polydispersed scattering features of the same shape, where the FWHM of the size distribution is  $\sim 20\%$ .

### 5.8.3.1.6. Particle pair density distribution function (PDDF)

All of the particle shapes considered in Section 5.8.3.1.5 model the scattering intensity *versus*  $Q$  as a Fourier transform of the scattering-particle (or feature) morphology. An alternative approach is to use an indirect Fourier transform method to extract the real-space function that gives rise to the scattering intensity (Glatter, 1977). This can then be interpreted in terms of the disordered scattering-feature morphology that may be present in the sample. For circularly symmetric small-angle scattering around the incident-beam direction, the particle pair density distribution function, PDDF or  $p(r)$ , is given by

$$p(r) = \frac{1}{2\pi^2} \int_0^\infty \frac{d\Sigma(Q)}{d\Omega} Qr \sin(Qr) dQ. \quad (5.8.24a)$$

Meanwhile

$$\frac{d\Sigma(Q)}{d\Omega} = 4\pi \int_0^\infty p(r) \frac{\sin(Qr)}{Qr} dr. \quad (5.8.24b)$$

We note that  $p(0) = 0$ , but

$$\frac{d\Sigma(0)}{d\Omega} = 4\pi \int_0^\infty p(r) dr = \Phi_V |\Delta\rho|^2 V_P. \quad (5.8.24c)$$

The inverse transform of equation (5.8.24a) is indirect in the sense that it must be carried out using an iterative inversion technique. Comparing equation (5.8.24b) with equation (5.8.2a), we note that the particle PDDF (which has units of  $\text{m}^{-2} \text{sr}^{-1}$ ) is related to the atomic pair correlation function by  $p(r) = n_P |\Delta\rho|^2 V_P r^2 \gamma(r) = \Phi_V |\Delta\rho|^2 r^2 \gamma(r)$ . Comparison with equation

## 5. DEFECTS, TEXTURE AND MICROSTRUCTURE

(5.8.16) indicates that  $\gamma(0) = 1 - \Phi_V$ , or for a dilute system  $\gamma(0) = 1$ . Meanwhile, the mean radius of gyration (or Guinier radius),  $R_G$ , of any particulate features present is given by

$$R_G^2 = \frac{\int_0^\infty p(r)r^2 dr}{2 \int_0^\infty p(r) dr}. \quad (5.8.25)$$

The main advantages of using the PDDF method in SAS studies are that the scattering morphology can be modelled directly in real space and that the  $p(r)$  function is essentially model-independent, so its use is tractable for a wide range of applications and analysis. Potential disadvantages are that (as with the scattering invariant) it is not possible to measure over the entire  $Q$  range required by the integral in equation (5.8.24a), so data must be extrapolated; and that the PDDF is affected by, and contains information on, any dispersion in the scattering feature size or shape. Whether it is preferable to model these effects in  $d\Sigma/d\Omega$  versus  $Q$  or  $p(r)$  versus  $r$  depends on the details of the scattering system.

### 5.8.3.1.7. Size distribution analysis

In the general case, SAS arises from scattering features that are not monodispersed in either shape or size. Frequently, it is not possible to distinguish polydispersity in shape from that in size as the SAS intensity profile is sensitive to variations in the dimensions of the scattering objects, whether coming from size or shape variation. For example, the scattering from a finite-width size distribution of spheroidal scattering objects with either  $\beta < 1$  or  $\beta > 1$  is identical to that from a different (broader) size distribution of spherical ( $\beta = 1$ ) objects. In most cases, the shape of the scattering features can be inferred from prior information, and so it is a size distribution of entities of a given shape that is sought from the scattering data. There are in general two ways of accomplishing this, and these are now described.

- (i) *Model size distributions.* One approach to size distribution analysis is simply to fit a size distribution,  $\varphi_s(R_O)$ , of an assumed functional form and average the scattering over the size distribution. For example, in the case of spheroidal scattering features, equation (5.8.18) becomes

$$\frac{d\Sigma}{d\Omega} = |\Delta\rho|^2 \int_0^\infty \phi_V(R_O) V_P(R_O) \frac{9\pi}{2} \int_0^1 \frac{[J_{3/2}(u)]^2}{u^3} dX dR_O, \quad (5.8.26)$$

where  $V_P(R_O)$  is the volume of features of radius  $R_O$ . The advantage of fitting an assumed model size distribution is that various weighted-average sizes of interest can be extracted analytically from the result. To illustrate this, a lognormal size distribution can be assumed with minimum, mode, median and mean radii given by  $R_{Omin}$ ,  $R_{Omode}$ ,  $R_{Omed}$  and  $R_{Omean}$ . If  $A(R_O) = (R_O - R_{Omin})/(R_{Omed} - R_{Omin})$ ,  $B_O = (R_{Omed} - R_{Omin})/(R_{Omode} - R_{Omin})$ , then

$$\begin{aligned} \phi_V(R_O) &= \frac{\Phi_V}{\{2\pi \ln(B_O)\}^{1/2}} \left( \frac{1}{R_O - R_{Omin}} \right) \exp \left\{ -\frac{[\ln A(R_O)]^2}{2 \ln(B_O)} \right\}, \end{aligned} \quad (5.8.27)$$

and several useful parameters can be extracted from the size distribution analytically. For example:  $R_{Omean} = R_{Omin} + \{B_O\}^{1/2}(R_{Omed} - R_{Omin})$ , the number-weighted mean radius,  $R_{ON}$ , is given by  $R_{ON} = R_{Omin} + \{B_O\}^{-1/2}(R_{Omode} - R_{Omin})$ ,

and the surface area per unit sample volume of the distribution  $S_V$ , is given by  $S_V = 3\Phi_V/R_{ON}$ . Obviously, other model size distributions may be appropriate in given situations, and corresponding expressions can be used for these and similar ensemble averages. In general, a fitted model size distribution permits differences in a material system to be quantified as a function of differences in processing or other conditions, using a relatively small number of parameters.

- (ii) *Size distributions using entropy maximization or other regularization.* An alternative approach to the least-squares fitting of a model function for the scattering-feature size distribution to the scattering data is to consider the contributions to the scattering intensity versus  $Q$ , from each histogram size bin within the size range of interest. In principle, the scattering contributions from each of the  $N$  size bins in a size distribution (assuming a given shape) can be treated as independent variables and fitted to the data by a least-squares method to determine the size distribution present. In practice, the large number of fitting parameters involved can make convergence to a unique solution, satisfying a good-fit  $\chi^2$  condition with respect to the measured data, difficult if not impossible. Furthermore, there is nothing to prevent unphysical negative regions from appearing in the fitted size distribution. Thus an additional constraint needs to be applied. Regularization methods link this second constraint to the minimum or required  $\chi^2$  condition via the use of a Lagrange multiplier. Two widely used additional constraints are either to require the size distribution to have maximum configurational entropy or to require that the size distribution is maximally smooth (free from oscillatory artifacts). In both cases, a major advantage is that the mathematical formulation is set up to ensure that the resulting size distribution is everywhere intrinsically positive.

The size distribution is assumed to extend over a finite scale range, associated with the SAS data, and to comprise a sufficiently large number of size intervals so as to capture the observable features in the size distribution. The size-interval increments are usually constant in linear size (relatively narrow population and a limited overall size range) or in logarithmic size (large dynamic range in the size of contributing features, and/or large range in the  $Q$  range investigated with constant  $\Delta Q/Q$  resolution). Using similar notation as in previous sections, if  $\varphi(R_i)$  is the value of the volume fraction distribution function for the  $i$ th size bin associated with size  $R_i$  (not necessarily  $R_O$  for a sphere or spheroid; any constant shape may be assumed), then the volume fraction in the  $i$ th size bin is  $f_i = \varphi(R_i)\Delta R_i$  where  $\Delta R_i$  is the width of the  $i$ th size bin. A configurational entropy,  $S_C$ , of the size distribution can then be defined in the convenient form

$$S_C = - \sum_{i=1}^N \frac{f_i}{h} \log \left( \frac{f_i}{h} \right), \quad (5.8.28a)$$

where  $h$  is a baseline constant (or a default distribution,  $h_i$ ), such that  $f_i/h$  is sufficiently large for Stirling's approximation to apply, i.e.  $\log[(f_i/h)!] = (f_i/h)\log(f_i/h) - (f_i/h)$ . (This is needed for all  $f_i$  of significance in the computing algorithm.) Note that the  $\log(f_i/h)$  term implies that the  $f_i$  components are all positive. Entropy-maximization algorithms then find the histogram size distribution,  $f_i$ , hence the differential size distribution  $\varphi(R_i)$ , that meets the requirement

$$S_C - L_S \chi^2 = \text{a maximum}, \quad (5.8.28b)$$

## 5.8. DISORDERED HETEROGENEOUS MATERIALS

where  $L_S$  is a Lagrange multiplier. Subject to the  $\chi^2$  requirement, analogous to the case in thermodynamics, the resulting maximum configurational entropy histogram distribution,  $f_i$ , is the most likely. However, because Bessel-function oscillations appear in the scattering from most assumed shapes for the scattering features, oscillations can still appear in the size distribution obtained, especially when this is a narrow distribution, despite applying the maximum entropy (*MaxEnt*) constraint (Potton *et al.*, 1988; Morrison *et al.*, 1992).

To find the smoothest size distribution consistent with the scattering data, it is necessary to define the roughness of the distribution,  $Z_C$ ,

$$Z_C = \sum_{i=1}^N (f_{i+1} - f_i)^2 + f_1^2 + f_N^2, \quad (5.8.29a)$$

and to satisfy the condition

$$Z_C + L_Z \chi^2 = \text{a minimum}, \quad (5.8.29b)$$

where  $L_Z$  is another Lagrange multiplier.

Although frequently applied to obtain scattering-feature size distributions, this method, simply referred to as regularization in SAS analysis, was applied originally to optimize the PDDF  $p(r)$  functions produced from SAS data via the indirect Fourier transform technique (Glatter, 1977, 1980). The maximum-entropy method has also been applied directly to derive PDDF  $p(r)$  functions.

### 5.8.3.1.8. Particle structure factor and interparticle interference effects

With the exceptions of the scattering invariant and the Debye–Bueche approximation, our discussion so far has assumed that the SAS intensity arises from a dilute, disordered ensemble of discrete scattering features (particles or pores). In the terminology of equation (5.8.2a) this implies that the particle structure factor  $S_P(Q) = 1$ . For many scattering morphologies, this assumption holds well for  $\Phi_V < \sim 0.05$  (or 5%), although the effects of higher concentration are frequently neglected for  $\Phi_V < \sim 0.10$ . However, once the volume fraction of the scattering features is significantly above this, interparticle interference effects, as expressed in the particle structure factor  $S_P(Q)$ , can be significant. In general, it can be shown that (Guinier & Fournet, 1955)

$$S_P(Q) = 1 + n_p \int_0^\infty [g_p(r) - 1] \frac{4\pi r^2 \sin(Qr)}{Qr} dr \quad (5.8.30a)$$

and

$$g_p(r) = 1 + \frac{1}{2\pi^2 n_p} \int_0^\infty [S_P(Q) - 1] \frac{\sin(Qr)}{Qr} Q^2 dQ, \quad (5.8.30b)$$

where  $g_p(r)$  is the dimensionless *particle* pair correlation function. Apart from the different normalization of equations (5.8.30a) and (5.8.30b) compared to equations (5.8.24b) and (5.8.24a), respectively, the slightly different form arises due to the exclusion volume around the centre of each scattering particle within which the centre of a neighbouring particle cannot approach. While this may not be strictly true for a population of voids or pores, it needs to be at least approximately true for a formalism assuming a concentrated population of discrete scattering features with well separated form-factor and structure-

factor terms. It should also be noted that the actual radial distribution function for neighbouring particles,  $Y_p(r)$ , with units of  $\text{m}^{-1}$ , is given by  $Y_p(r) = 4\pi r^2 n_p g_p(r)$ .

In principle, equations (5.8.30a) and (5.8.30b) permit  $g_p(r)$  and  $Y_p(r)$  to be determined from an experimentally determined  $S_P(Q)$ , which in turn is extracted from  $d\Sigma/d\Omega$  versus  $Q$  by dividing  $d\Sigma/d\Omega$  by the known or assumed  $n_p |\Delta\rho|^2 V_p^2 F_p^2(Q)$  or  $\Phi_V |\Delta\rho|^2 V_p F_p^2(Q)$ . The actual situation is complicated if any finite dispersion in the scattering feature size is present. The  $S_P(Q)$  term in equation (5.8.2a) should then be replaced by  $S_1(Q)$  where for a hard-sphere Percus–Yevick model (Percus & Yevick, 1958)

$$S_1(Q) = 1 + B_P(Q)[S_P(Q) - 1] \quad (5.8.31a)$$

and

$$B_P(Q) = \frac{|F_P(Q)|^2}{|F_P(Q)|^2}. \quad (5.8.31b)$$

Depending on how broad the size dispersion actually is, an interparticle interference may not be apparent in the scattering data. Nevertheless, the effects of high concentration [deviation of  $S_P(Q)$  from 1] may still be significant.

### 5.8.3.1.9. Fractal models

Fractal scattering morphologies, despite generally being disordered in nature, are defined by their scale invariance and give rise to non-integral power laws in small-angle scattering. Examples of material systems incorporating fractal morphologies tractable for analysis by SAS methods abound, and include molecular sieves (Pauly *et al.*, 1999), dendrimers (Scherrenberg *et al.*, 1998), nanoparticle–polymer nanocomposites (Jouault *et al.*, 2009), aerogels (Emmerling & Fricke, 1992), crystallization phenomena (de Moor *et al.*, 1997), nanoparticle aggregates in flames (Hyeon-Lee *et al.*, 1998), Stober nanoparticle ensembles (Green *et al.*, 2003), cements and porous rocks (Allen, 1991), and asphaltene suspensions (Roux *et al.*, 2001). In some of these systems the solid phase, *e.g.* an assembly of nanoparticles, obviously forms the fractal morphology; in other systems, *e.g.* porous rocks, it may be the porous void network that constitutes the primary fractal morphology.

(i) *Mass- or volume-fractal morphologies.* In the case of a mass- or volume-fractal morphology, the mass and volume of the scattering features within a radius  $r$  of any one point in the morphology scales not with  $r^3$ , but with  $r^{D_V}$  where  $D_V < 3$ . The associated scattering power law can be shown to be  $Q^{-D_V}$ . For a contiguous scattering phase  $D_V \geq 1$ .  $D_V = 1$  indicates a 1D chain structure and  $D_V = 3$  indicates a space-filling phase with no fractal dependence. Thus  $1 \leq D_V \leq 3$  for volume-fractal morphologies. However,  $D_V = 2$  indicates a sheet-like structure, and  $D_V < 2$  can be associated with a 2D fractal structure within an overall sheet-like morphology. So for three Euclidean dimensions  $2 \leq D_V \leq 3$ . Generally there is a maximum length scale, the correlation length  $\xi_V$ , over which volume-fractal scaling applies, and there is also a minimum length scale associated with the smallest scattering features that make up the fractal morphology. In the case of solid features of radius  $R_O$ , the minimum possible dimension for fractal scaling is the correlation hole radius,  $R_C = 2R_O$ , the minimum separation distance for centres of neighbouring particles. With a local packing fraction of  $\eta$  assumed within the correlation hole radius, and approximating the normalization to give extrapolation to  $Q = 0$  consistent with a

## 5. DEFECTS, TEXTURE AND MICROSTRUCTURE

Guinier approximation for the fractal structure (Freltoft *et al.*, 1986),

$$\frac{d\Sigma}{d\Omega} = \Phi_V |\Delta\rho|^2 V_p \left[ \frac{\eta R_C^3}{R_O^3} \left( \frac{\xi_V}{R_C} \right)^{D_V} \times \left( \frac{\sin[(D_V - 1) \arctan(Q\xi_V)]}{[1 + (Q\xi)^2]^{(D_V-1)/2} (D_V - 1) Q\xi_V} \right) + (1 - \eta)^2 \right] F^2(Q), \quad (5.8.32)$$

where  $\Phi_V$  is the total volume fraction of the scattering features, here assumed to be spheres of volume  $V_p = 4\pi R_C^3/3$  with scattering form factor  $F^2(Q)$  that comprise the volume-fractal microstructure. The trigonometric terms refer to angles in radians and the arctangent angle is in the principal range from zero to  $\pi/2$ . This expression exhibits  $Q^{-D_V}$  scattering in the  $Q$  range  $\xi_V^{-1} \ll Q \ll R_O^{-1}$ , single-particle form-factor scattering in the range  $Q \geq R_O^{-1}$  (including Porod  $Q^{-4}$  scattering for  $Q \gg R_O^{-1}$ ), and the scattering  $Q$ -dependence ‘tops out’ for  $Q \leq \xi_V^{-1}$ . Volume-fractal SAS data can be fitted using this function with  $\Phi_V$ ,  $R_O$ ,  $D_V$ ,  $\xi_V$  and  $\eta$  as fitted parameters (plus a flat background term if needed). However, it must be emphasized that this can only be done if the data can be measured over a sufficient  $Q$  range and with sufficient  $Q$  resolution for the different scattering regimes indicated to be apparent in the data. If this condition is not met, other prior knowledge must be used to constrain the fitting parameters. Otherwise, equation (5.8.32) cannot result in convergence to a unique solution. This is particularly the case when other morphology components are present, such as surface-fractal scattering.

- (ii) *Surface-fractal morphology.* Any rough interface between two phases exhibits the property that its measured surface area increases when additional roughness at finer length scales is included. Surface-fractal roughness occurs when a fixed exponent links the surface-area value to the inverse of the roughness scale considered. A true surface fractal involves roughness in all three dimensions with a convoluted surface topology that includes re-entry (doughnut-like) geometries. However, when the chord length across strands of the structure is comparable with the roughness scale being considered ( $Q^{-1}$ ), SAS ‘sees’ this as a 3D structure, not as a rough 2D interface. For SAS applications, surface-fractal morphology is limited to an interface with self-affine 2D roughness that, otherwise, can be considered essentially planar in nature. Within this limitation, a surface fractal occurs when the number of surface elements of area  $\Delta S(r)$  needed to cover an interface with roughness included down to a length scale  $r$  scales as  $r^{-D_S}$  where  $D_S \geq 2$ . We note that a smooth interface has  $D_S = 2$ . Once again, we assume that there is a maximum length scale or correlation length,  $\xi_S$ , over which the fractal roughness occurs, usually related to the size of the (large) features that possess the interface with fractal surface roughness. Generally,  $\xi_S$  can be associated with the geometrically smooth surface area,  $S_O$ . With these terms defined, a full expression for surface-fractal scattering can be derived using a generalization of Porod’s law (Bale & Schmidt, 1984):

$$\frac{d\Sigma}{d\Omega} = \frac{\pi \xi_S^4 |\Delta\rho|^2 S_O \Gamma(5 - D_S) \sin[(3 - D_S) \arctan(Q\xi_S)]}{[1 + (Q\xi_S)^2]^{(5-D_S)/2} Q\xi_S}, \quad (5.8.33)$$

where  $\Gamma(5 - D_S)$  refers to the Gamma function. When  $D_S = 2$ , equation (5.8.33) reduces to the Porod expression of equation (5.8.15). For a self-affine surface-fractal interface  $2 \leq D_S \leq 3$ , and the expression exhibits a  $Q^{-(6-D_S)}$  power law for  $Q \gg \xi_S^{-1}$ . Again the scattering intensity ‘tops out’ for  $Q \leq \xi_S^{-1}$ . Unlike the approximate normalization at low  $Q$  provided by equation (5.8.32) for a volume-fractal morphology, the normalization at low  $Q$  provided by equation (5.8.33) for a self-affine surface-fractal morphology is exact. Equation (5.8.33) can be used fit to experimental data using three parameters:  $S_O$ ,  $D_S$  and  $\xi_S$ . A further term like that used in equation (5.8.32) can be introduced to deal with the scattering at high  $Q$ . Alternatively, some other morphology such as volume-fractal scattering (power law between  $Q^{-2}$  and  $Q^{-3}$ ) may take over from the steeply declining surface-fractal scattering (power law between  $Q^{-3}$  and  $Q^{-4}$ ), and it may not be necessary to truncate the surface-fractal scattering at high  $Q$ . For a minimum roughness scale,  $R_O$ , where surface-fractal scaling applies, the fully rough surface area,  $S_{SF}$ , is related to the geometrically smooth surface area,  $S_O$ , by  $S_{SF} = S_O (\xi_S/R_O)^{(D_S-2)}$ .

Particularly if volume- and surface-fractal morphologies coexist, it is essential that SAS data cover sufficient  $Q$  range (*e.g.*,  $\xi_V^{-1} < Q < R_C^{-1}$  for a volume fractal) with sufficient  $Q$  resolution, and that sufficient parameter constraints based on prior knowledge be applied, to achieve convergence to a unique solution. In practice, fractal microstructures being hierarchical in nature, SAS data over three to four decades in  $Q$ , and perhaps eight or nine decades in intensity, are required. Despite these conditions, once an acceptable model paradigm is implemented, fractal models offer the advantage of combining single-feature scattering, dispersion effects and concentrated morphology issues into a single approach for fractal disordered systems.

In this and previous sections, we have considered physical microstructure models that produce the scattering observed. How well any one physical model can fit the data depends, at least to some extent, on how well the microstructure assumed approximates to that actually present. Unfortunately, while misfits should occur if the wrong model is assumed, they can also occur if the correct basic model is assumed but the actual situation is less idealized than the model implies, or if the data-point density and weighting *versus*  $Q$  make fitting of the SAS profile function mathematically ill-conditioned. One approach to addressing this situation is to develop a hierarchical nest of numerical fitting functions for SAS data that can achieve good and stable fits over a large  $Q$  range and for many situations. Having obtained a good fit, the SAS interpretation problem is then transferred to developing a credible physical interpretation of the mathematical fit parameters obtained. An obvious disadvantage is that the mathematical parameters can be misinterpreted. Nevertheless, one such approach that has met with considerable success in recent years, especially in the analysis of SAS data from polymer systems, is the ‘unified fit’ model developed by Beaucage (1995).

### 5.8.3.1.10. Anomalous SAXS and contrast-variation SANS

Intrinsic wide-angle and small-angle scattering intensities arise from the X-ray atomic scattering form factors, or the neutron nuclear scattering lengths (*i.e.*,  $b_i$ ,  $b_j$ ) for the various atomic species within a material. In diffraction, these are manifested in summations such as given in equation (5.8.6). In SAXS or SANS, the scattering contrast factors,  $|\Delta\rho|^2$ , derived from the scattering-

## 5.8. DISORDERED HETEROGENEOUS MATERIALS

length densities, determine the intrinsic strength of the scattering, as indicated in equation (5.8.2a). In many materials that are partially disordered and/or heterogeneous, several measurements involving both X-rays and neutrons may be desirable to determine the compositions, densities and phases of the components giving rise to the scattering. However, in both X-ray and neutron measurements, it is possible to vary the scattering lengths and contrast factors in order to interrogate the various scattering components within a single set of measurements. For WAXS and SAXS, this can be done at an X-ray synchrotron by varying the X-ray energy just below the absorption-edge energy for an atomic species present in a material of interest. For WANS and SANS, the neutron isotope effect is exploited by varying the isotope mix of one of the constituents present in the sample material, *e.g.*, H<sub>2</sub>O/D<sub>2</sub>O contrast variation. While these effects can be exploited in both diffraction and small-angle scattering, here we concentrate on SAXS and SANS.

(i) *Anomalous SAXS*. Just below the X-ray energy for resonant absorption by an atom of a given element (a characteristic absorption edge, obtainable from published tables, but also measurable at synchrotron sources by careful tuning of the X-ray energy using calibration absorption foils), the X-ray form factor,  $b_i$ , deviates significantly from its normal (non-resonant) value measured at X-ray energies far from an absorption edge (Thompson, 2009). Consequently, the X-ray scattering contrast factor  $|\Delta\rho|^2$  applicable to SAXS measurements of any heterogeneous scattering features incorporating the given element also varies (anomalously) with the X-ray energy. Fundamental derivations of resonant-scattering contrast factors and their formal incorporation into the interpretation of anomalous SAXS (ASAXS) measurements are described in detail elsewhere (Cromer & Liberman, 1970; Hoyt *et al.*, 1984). For the purpose of ASAXS measurements of heterogeneities in disordered materials, it suffices to apply the following approximate relationship between the energy-dependent SAXS contrast factor,  $|\Delta\rho(E)|^2$ , and the X-ray energy,  $E$ , when this is below the absorption energy,  $E_0$ , by a few tens of eV:

$$|\Delta\rho(E)|^2 = |\Delta\rho|_{NR}^2 + A_{E_0} \ln\left(\frac{E_0 - E}{E_0}\right), \quad (5.8.34)$$

where  $|\Delta\rho|_{NR}^2$  is the scattering contrast factor at X-ray energies far from the absorption edge and  $A_{E_0}$  is a scattering contrast constant for the specific material and absorption energy of interest. Note that the  $\ln[(E_0 - E)/E_0]$  factor is strongly negative and ASAXS measurements must be made at  $E < E_0$  because of the large decrease in sample transmission for  $E > E_0$  as a result of the large increase in resonant X-ray absorption by the sample at  $E = E_0$ . While  $|\Delta\rho|_{NR}^2$  is always positive,  $A_{E_0}$  is positive when the electron density is higher in the phase containing the element associated with the X-ray absorption edge, resulting in a decrease in scattering contrast with X-ray energy as the absorption-edge energy  $E_0$  is approached from below. However,  $A_{E_0}$  is negative when the electron density is lower in the phase containing the X-ray-absorption-edge element, resulting in an increase in scattering contrast with X-ray energy as the absorption edge is approached from below. While ASAXS contrast variation with energy can be subtle, its careful measurement close to appropriate X-ray absorption edges can provide important insights into the composition and density of heterogeneities in disordered materials (Allen *et al.*, 2014).

(ii) *Contrast-variation SANS*. The strong isotope effect in neutron scattering lengths (Sears, 1992), together with the sensitivity of neutrons to hydrogen in hydrogenous materials, which are frequently disordered, makes these materials prime targets for investigation by contrast-variation SANS. Taking H<sub>2</sub>O/D<sub>2</sub>O contrast variation as an example, the neutron scattering-length density of H<sub>2</sub>O is given by  $\rho_H = -0.56 \times 10^{14} \text{ m}^{-2}$ , while for D<sub>2</sub>O  $\rho_D = +6.40 \times 10^{14} \text{ m}^{-2}$ . Since H<sub>2</sub>O, HDO and D<sub>2</sub>O are completely mixable at the atomic level, the scattering-length density of an H<sub>2</sub>O/D<sub>2</sub>O mix can be interpolated between these two end points for any molar mix of H<sub>2</sub>O and D<sub>2</sub>O. Furthermore, most solid hydrogenous materials have scattering-length densities between  $\rho_H$  and  $\rho_D$ . Thus, if the SANS is measured for a series of porous samples containing various H<sub>2</sub>O/D<sub>2</sub>O mixes in the pore water, the absolute-calibrated SANS intensity profile of  $d\Sigma/d\Omega$  *versus*  $Q$  should remain the same as a function of D/H ratio, except that the absolute intensity across the  $Q$  range will follow a parabola in  $|\Delta\rho|^2$ , going to zero at the contrast match point where the scattering-length density in the pore water matches that of the solid phase. For a genuine two-phase system (one solid phase plus the pore fluid), the contrast match point can be found by plotting the square root of the intensity *versus* the molar fraction of D<sub>2</sub>O, with negative values on the H<sub>2</sub>O side of the estimated match point and positive values on the D<sub>2</sub>O side. A straight-line fit then gives the match point as the intercept on the horizontal axis.

The situation is more complicated when more than one solid phase is present, as each solid phase has its own contrast-variation parabola with the pore fluid. The weighted sum of these parabolas is still a parabola, but now there is a contrast minimum with finite residual intensity (no one phase matched) at the minimum. If some of the solid phases have known composition and density, it may be possible to subtract these out, leaving a contrast-match curve for an unknown phase. Another complication occurs when the H<sub>2</sub>O/D<sub>2</sub>O exchange does not occur uniformly at all length scales. A decision must then be made as to which scale (and hence  $Q$ ) to apply the contrast-variation analysis to. It is also possible to apply contrast-variation analysis to hydrogenous systems formed using various H/D isotope mixes, but care must be taken to ensure that the H/D exchange does not affect the reaction times which, despite the chemical equivalence of the hydrated and deuterated components, is not always the case. Despite these issues, SANS contrast-variation measurements play an important role in the investigation of heterogeneous and disordered materials, especially where a lack of crystallinity in one or more critical phases precludes many other diffraction-based analyses, as in the case of polymers or cements (Allen *et al.*, 2007).

### 5.8.3.1.11. Magnetic SANS analysis

As mentioned earlier in Section 5.8.2, neutrons, having a magnetic moment themselves, interact with atoms that also have a net magnetic moment. Much of what we know about magnetism or magnetic phenomena within materials has been discovered through magnetic neutron scattering and diffraction, *e.g.*, Ritter *et al.* (1997) (see also Chapter 2.8). Here, we add brief comments mainly regarding magnetic SANS analysis of heterogeneous magnetic materials. Even in a material containing atoms or molecules possessing net magnetic moments, there is no magnetic

## 5. DEFECTS, TEXTURE AND MICROSTRUCTURE

SANS intensity if these magnetic moments are randomly oriented (although there may be a contribution to the incoherent flat background scattering). However, if magnetic ordering is present (ferromagnetic, antiferromagnetic, ferrimagnetic *etc.*), and if an axis of magnetic alignment is established, *e.g.* by applying a saturation magnetic field to align the atomic magnetic moments (or those of any magnetic domains present), an anisotropic magnetic SANS contribution can be measured. The magnetic SANS intensity varies as  $\sin^2 \alpha$ , where  $\alpha$  is the angle between the direction of the neutron magnetic moment and that of the sample (*i.e.*, that of the applied magnetic field). Analysis of the anisotropic intensity collected using a 2D PSD allows the anisotropic ( $\sin^2 \alpha$ ) magnetic SANS component to be separated from the (usually isotropic) nuclear SANS component.

Once the anisotropic nature of the magnetic SANS data is allowed for, the full set of analyses discussed previously in Section 5.8.3 can be applied, using the magnetic SANS contrast factors in place of the non-magnetic contrast factors, to model and quantify magnetic microstructures and heterogeneities that are present. Significant magnetic SANS studies have included precipitation phenomena in ferritic steels (Allen *et al.*, 1993; Mathon *et al.*, 2003), the magnetic structure of nanocrystalline iron (Wagner *et al.*, 1991), polarons in perovskites (De Teresa *et al.*, 1997) and flux-line lattice behaviour in superconductors (Yaron *et al.*, 1995; Riseman *et al.*, 1998). Magnetic SANS investigations have been made even more powerful by the development of polarized SANS instrumentation (SANSPOLE) that uses supermirrors to provide significant polarization of the incident neutron beam (Zhao *et al.*, 1995). The spin-dependent scattering of polarized neutrons enables models for heterogeneous magnetic structures to be more finely tuned, as well as providing a better separation of the magnetic and non-magnetic scattering components in the experimental data (Heinemann & Wiedenmann, 2003; Mettus & Michels, 2015).

Finally, it should be mentioned that neutron-polarization analysis has been extended well beyond the magnetic SANS regime. Following the development of the neutron spin-echo technique by Mezei and others in the 1970s (Mezei, 1980), spin-echo SANS (SESANS) instruments have been designed to compare the neutron polarization before and after the sample position, and measure changes in the Larmor precession angle of the neutron polarization plane as neutrons traverse a sample. Although the analysis can be complex and goes beyond the scope of this chapter, this technique, which is applicable to all classes of sample systems, not just magnetic samples, can provide unique information on the dynamics of an ensemble system (including biological systems), as well as structural information over a length scale that overlaps with USANS (Rekvelde, 1996).

### 5.8.3.1.12. Further analysis of X-ray reflectivity and GI-SAXS

Some further discussion is warranted of disorder that can occur at surfaces and interfaces in materials, or within thin films:

- (i) *Parratt function reflectivity profile* (Parratt, 1954). Assuming specular reflectivity  $R(Q)$  versus  $Q$  data have been obtained and corrected as discussed previously, these can be analysed to give a density profile of a series of  $N$  thin-film layers on a substrate, together with a representation of the roughness/diffuseness associated with each film boundary. Assuming a scattering-length density  $\rho(z)$  as a function of overall distance  $z$  below the mean position of the top surface of the whole sample,

$$\rho(z) = \rho_0 + \sum_{m=1}^{N+1} \frac{(\rho_m - \rho_{m-1})}{2} \left[ 1 + \operatorname{erf} \left( \frac{z - z_m}{\sigma_m \sqrt{2}} \right) \right], \quad (5.8.35)$$

where  $z_m = \sum_{k=1}^{m-1} \tau_k$ ,  $\rho_0$  is the scattering-length density above the top film layer (frequently  $\rho_0 = 0$  unless the film interfaces are buried in some other bulk material or are immersed in a liquid),  $\rho_m$  is the scattering-length density in the  $m$ th film layer,  $\operatorname{erf}(x)$  is the error function,  $\sigma_m$  is the standard deviation of the roughness (or diffuseness) for the  $m$ th interface at the top of the  $m$ th film (where the first interface at  $z_1 = 0$  defines the top of the whole assembly), and  $z_m$  is the mean location of the  $m$ th interface and is the sum of the thicknesses,  $\tau_k$ , of each film above the  $m$ th interface and film. Note that the final  $(N + 1)$ th interface is with the substrate and  $z_{N+1}$  is the combined thickness of all of the films.

Practical refinement of the density profile by fitting the predicted reflectivity curve to experimental reflectivity data must take into account corrections not only for overall sample geometry but also for instrumental resolution corrections *etc.* However, the reflectivity curve  $R(Q)$  for a series of thin films on a substrate, as described above, can in principle be compared to the Fresnel reflectivity curve,  $R_F(Q)$ , from a perfectly smooth, bare substrate of scattering-length density  $\rho_{N+1}$ , here denoted  $\rho_{\text{SUB}}$ , by (Als-Nielsen, 2001)

$$\frac{R(Q)}{R_F(Q)} = \left| \frac{1}{\rho_{\text{SUB}}} \int_{-\infty}^{\infty} \exp(iQz) \left( \frac{d\rho}{dz} \right) dz \right|^2, \quad (5.8.36)$$

where the integral range must be extended out in both directions until  $d\rho/dz = 0$ .

Note that specular reflectivity studies can detect a rough or diffuse boundary between successive films, but cannot themselves differentiate between the two. This said, neutron contrast-variation methods may sometimes be used to interrogate the composition at an interface (Nelson, 2006). However, in most cases, non-specular reflectivity or GI-SAXS measurements must be used to investigate the nature of the disorder occurring at the film interfaces (or within films), or to characterize in-plane structures parallel to the substrate.

- (ii) *Distorted-wave Born approximation (DWBA)*. In Section 5.8.2.4 the case of GI-SAXS or NS-SANS from a microstructure within a single thick film was discussed and the various refraction corrections considered. However, in the more general case of thin films where  $\zeta_{\text{mean}} \geq \tau_{\text{film}}$ , at least four different contributions to the scattering must be considered: (i) a single scattering event as discussed in Section 5.8.2.4; (ii) a single scattering event, followed by reflection from the film/substrate interface; (iii) reflection from the film/substrate interface, followed by a single scattering event; and (iv) as (iii) but with a further reflection from the film/substrate interface and possibly a further scattering event. To some extent component (i) can be separated from (ii) to (iv), corrected for refraction effects and interpreted using the Born approximation. However, for a full treatment of GI-SAXS data from thin films where components (ii) to (iv) cannot be ignored, distortions from the incident plane wave assumed in the Born approximation must be allowed for in what is effectively a superposition of the four compo-

## 5.8. DISORDERED HETEROGENEOUS MATERIALS

nents – hence, the use of the DWBA (Sinha *et al.*, 1988; Rauscher *et al.*, 1995). Because of this, the DWBA does not simply provide a modified form of  $d\Sigma/d\Omega$  that takes into account all of the corrections involved, but it also modifies the form factors and structure factors associated with the underlying microstructural features within a film.

It is not practical to give a full exposition of the DWBA in the context of this chapter. Fortunately, it can be shown that the DWBA only has a significant effect for incidence and scattering grazing angles,  $\theta_i$  and  $\theta_s$ , close to the critical angle  $\theta_C$ . Furthermore, software tools are now publicly available that address the analysis needs for most of the main cases of interest. We refer the interested reader to the various references and software available: Lazzari (2002), Babonneau (2010) and Korolkov *et al.* (2012), the last of which is focused on GI-SANS.

### 5.8.3.2. Small-angle scattering effects on wide-angle scattering analysis

In Section 5.8.2.5, it was pointed out that the determination of the real-space atomic pair density distribution function,  $G(r)$ , from wide-angle scattering (diffraction) is affected by the non-measurable scattering contribution close to  $Q = 0$ . For a macroscopic diffracting sample volume, the missing scattering is effectively at infinitesimal  $Q$ , and its absence from the Fourier transform integral of equation (5.8.10) results in the negative term  $-4\pi r n_0$  appearing in the expression for  $G(r)$ . We now consider the case where the diffracting regions giving rise to the wide-angle scattering (whether internally crystalline or atomically disordered) are, themselves, randomly distributed particles of nanoscale size within a solid matrix or liquid medium. The finite size of the particles now contributes measurable small-angle scattering at low  $Q$ . If this is not measured, a more complex negative term appears in the expression for  $G(r)$  determined from a Fourier transform of the total-scattering data measured in the wide-angle regime.

In general it can be shown that equation (5.8.13) for the atomic pair density distribution function,  $G(r)$ , can be modified to become (Cargill, 1971; Farrow & Billinge, 2009)

$$G(r) = 4\pi r [n(r) - \gamma_0(r)n_0], \quad (5.8.37)$$

where  $n(r)$  is the atomic number density distribution at all  $r$  with respect to any given atom,  $n_0$  is the mean atomic number density and  $\gamma_0(r)$  is the dimensionless atomic pair correlation function of equations (5.8.2a,b). While  $\gamma_0(r)$  can be determined empirically from calibrated SAXS or SANS data, it can also be defined in terms of an individual small-angle scattering particle (Porod, 1951; Guinier & Fournet, 1955; Glatter & Kratky, 1982). Let  $c(\mathbf{r})$  be a shape function with the property that  $c(\mathbf{r}) = 1$  for  $\mathbf{r}$  inside the particle and  $c(\mathbf{r}) = 0$  for  $\mathbf{r}$  outside the particle. Then for any given particle orientation

$$\gamma_0(\mathbf{r}) = \frac{1}{V_p} \int_0^\infty c(\mathbf{r})c(\mathbf{r} + \mathbf{r}') d\mathbf{r}' \quad \text{and} \quad \int_0^\infty \gamma_0(\mathbf{r}) d\mathbf{r} = V_p, \quad (5.8.38)$$

where for randomly oriented particles, such as would give an isotropic microstructure, the orientational average of  $\gamma_0(\mathbf{r})$  is  $\gamma_0(r)$ . For nanoscale small-angle scattering particles, we note that  $\gamma_0(r) = 0$  for  $r$  greater than the largest chord dimension of the scattering particle. This gives the characteristic shape of the  $G(r)$  component shown in Fig. 5.8.6(c) when scattering in the SAS regime ( $Q < Q_{\min}$ ) is not measured in total-scattering measurements. However, when the total scattering is measured for a very

dilute ensemble of nanoparticles, the  $G(r)$  function itself becomes featureless for  $r$  greater than the largest chord length of the scattering particles, as has been demonstrated experimentally (Proffen & Kim, 2009). Meanwhile, we also note that when  $r$  is very much less than the maximum chord dimension of the particles, such as is always the case when the particles are macroscopic in size,  $\gamma_0(r) = 1$  and equation (5.8.37) reverts to equation (5.8.13).

### 5.8.3.3. Combining information from different methods

Increasingly, several diffraction-based techniques are being used together to interrogate disordered or partially disordered material systems. A major example offered here is the combination of SAXS or SANS at low  $Q$  with diffraction-based total-scattering methods at larger  $Q$ , or wide-angle scattering. In order to account fully for the SAS contribution in total-scattering data, or simply to combine diffraction and SAS data, it is necessary to inter-calibrate the scattered and diffracted intensities between the techniques. In this connection, it is important to allow for the different conventions in normalizing the scattered or diffracted intensities.

In SAXS or SANS, the macroscopic differential scattering cross section,  $d\Sigma/d\Omega$ , is used to give the normalized intensity, as defined in Section 5.8.2. In diffraction, the coherent diffraction intensity,  $I_{\text{coh}}$ , is used as defined in equation (5.8.6), with  $I_{\text{coh}}$  derived from a coherent sum of the diffraction amplitudes from all of the diffracting atoms sampled. In equation (5.8.6) it is assumed that the scattering is normalized to an incident beam comprising a plane wave of unit amplitude (hence unit intensity), and that the individual contributions to the scattered wave are also normalized per unit solid angle. Thus, the additional normalization required to convert  $I_{\text{coh}}$  to  $d\Sigma/d\Omega$  is with respect to the sample volume and  $d\Sigma/d\Omega = I_{\text{coh}}/V_S$ . However, whereas the SAS expressions are based on the assumption that the SAXS or SANS intensity is small compared with the incident-beam intensity, this assumption does not necessarily hold for WAXS or WANS.

In practice, the quantitative comparison of SAXS and SANS intensities with those of WAXS and WANS can be complicated by a number of factors. Crystalline structure factors summed over significant coherently diffracting sample volumes can lead to extinction effects that affect the Bragg diffraction peak intensities. Similarly, the peak intensities can also be affected by crystalline texture, or by the presence of stress and strain. All these issues are discussed in Chapters 5.2 and 5.3, but they are less likely to have a significant effect for a partially disordered material having weak diffraction peaks, which is of most interest here. Two effects that do influence any quantitative comparison of the small- and wide-angle scattering from disordered materials are those due to thermal diffuse scattering (WAXS, WANS, total scattering) and multiple scattering (SAXS and SANS).

Thermal diffuse scattering (TDS) reduces the intensity of the diffraction peaks measured in WAXS or WANS and redistributes it to the background scattering between the peaks. The functional form of the latter depends on the details of the material in question, and this can be further complicated in the case of disordered or partially disordered materials in the context of total-scattering measurements. However, the reduction in coherent Bragg peak intensity and its effect on the determination of  $G(r)$  can be treated by a modification of equation (5.8.8) to allow for the effect of the Debye–Waller factor (Farrow & Billinge, 2009):

$$S(Q) - 1 = \left( \frac{1}{N\langle b \rangle^2} \right) \sum_{i \neq j} b_i^* b_j \left[ \frac{\sin(Qr_{ij})}{Qr_{ij}} \right] \exp\left( -\frac{\sigma_{ij}^2 Q^2}{2} \right), \quad (5.8.39)$$

where  $\sigma_{ij}^2$  is the correlated Debye–Waller broadening factor (in real space) for the  $i$ - $j$ th atom pair. The  $\sigma_{ij}^2$  term includes the expected Arrhenius dependence on the absolute temperature,  $T$ .

Multiple scattering in SAXS or SANS reduces the scattering intensity at the lowest  $Q$  values measured and redistributes the lost intensity to higher  $Q$  values. However, without correction, this effect can be masked by an incorrect sample transmission  $T_S$ , used in place of  $T_{SS}$ , in equation (5.8.4) for the intensity calibration. The multiple-scattering correction outlined in Section 5.8.2.3.3 must be applied before combining SAXS or SANS data with WAXS or WANS. Obviously, it is necessary to integrate the scattering intensity out to a  $Q$  value beyond which multiple scattering can be ignored. (A decrease in apparent intensity of one decade from that at  $Q = 0$  suffices in most cases.) As indicated previously, this correction, alone, does *not* correct for the distortion in the SAS profile at low  $Q$  where multiple scattering is significant, but it *does* correct the calibrated  $d\Sigma/d\Omega$  for all higher  $Q$  values. Multiple-scattering corrections that include correcting some of the distortions in the SAS profile at low  $Q$  have been treated by Schelten & Schmatz (1980).

Assuming that corrected absolute scattering intensities can be attained, there are strong advantages in comparing these for WAXS and WANS, SAXS and SANS across corresponding  $Q$  ranges for partially disordered systems, especially where spatial variations in composition exist. To achieve this, the X-ray and neutron measurements need to be made on samples that are as closely identical to each other as possible, although the sample thickness and volume for neutrons must frequently be larger than for X-rays. A ratio of the WAXS/WANS integrated diffraction peak intensities for corresponding Bragg peaks provides a test of the diffracting unit cell composition of the crystalline component of a partially disordered material. This is because the values of the  $b_i$  and  $b_j$  for different atoms in the corresponding summations of equation (5.8.6) for X-rays and neutrons are different, allowing the predicted structural composition of a crystalline phase to be tested against experiment. Meanwhile, the ratio of the calibrated SAXS/SANS intensities over corresponding  $Q$  ranges provides a similar test of the overall composition and density of heterogeneities within the microstructure, regardless of whether the solid phase is crystalline or amorphous. Again, this is because the contrast factor  $|\Delta\rho|^2$  in equation (5.8.2a) is different for X-rays and neutrons (Thompson, 2009; Sears, 1992), depending on the composition and density both of the small-angle scattering heterogeneities and of the surrounding medium. The proportionality between the X-ray form factor and atomic number for X-ray scattering *versus* the strong isotope effect for neutron scattering can lead to very different sensitivities of X-rays and neutrons to different components in a disordered heterogeneous material system. This is particularly true when disordered hydrogenous species are present, some bound into the solid matrix, not all of which is crystalline. Clearly, the use of H/D contrast methods in WANS and SANS discussed in Section 5.8.3.1.10 can be strongly complemented by a comparison between the X-ray and neutron intensities.

Finally, we note the importance of relating the WAXS and SAXS and/or WANS and SANS results. In previous sections, we have shown the importance of accounting for the small-angle

scattering in total-scattering measurements of partially disordered material systems. With the added complications of needing to treat thermal diffuse scattering and other defect-related corrections to the scattering observed, the advantages of working independently with both the X-ray scattering form factors and contrast factors, and the corresponding neutron scattering-length densities and contrast factors, are that the entire interpretation scheme can be independently checked using two sets of scattering parameters. Again we emphasize the value of such an approach when hydrogenous components are present in a partially disordered heterogeneous material system.

#### 5.8.4. Prospects for future development and recommended further reading

At the present time, rapid advances are taking place in the diffraction- and scattering-based analysis of partially disordered and heterogeneous materials. What follows is a very brief summary of some of the more promising current developments.

##### 5.8.4.1. Developments at X-ray synchrotron facilities

New third-generation X-ray synchrotron facilities continue to come on line to serve the full range of diffraction- and spectroscopy-based techniques for investigating phenomena in new materials. Among these is the application of increasingly ambitious instrumentation using high X-ray energies for total-scattering analysis of nanocrystalline and disordered or partially crystalline materials over a large  $Q$  range (Petkov *et al.*, 2013). Instrumentation has also been developed to combine methods such as USAXS, SAXS and WAXS (including atomic pair density distribution analysis) to provide both microstructure and structure data for given samples within a single set of measurements (Becker *et al.*, 2010). Where possible, the X-ray energy range is being extended to higher energies to allow investigation of thicker or denser, more complex materials (Ilavsky *et al.*, 2012). At the same time, the increasingly higher X-ray fluxes available are allowing better time resolution and the more direct *in situ* studies of complex processes involving disordered materials. These instrumental developments include both bulk sample measurements using transmission geometry, and surface and thin-film measurements using a reflection geometry. As the need has increased for *in situ* studies of processes occurring within material systems, rather than just structural and microstructural measurements of materials under static conditions, so has interest in combining methods such as SAXS with techniques such as X-ray photon correlation spectroscopy (XPCS) to measure the equilibrium and non-equilibrium dynamics of phenomena occurring within materials (Zhang *et al.*, 2011). In this connection, the recent development of X-ray free-electron laser (FEL) coherent scattering (LCS) or fourth-generation X-ray sources is likely to play a major role in the future (Saldin *et al.*, 2011), as will the ongoing development of multi-bend achromat (MBA) diffraction-limited storage rings at synchrotrons (Tavares *et al.*, 2014). The coherent aspects of these new X-ray sources will affect all areas of X-ray scattering and diffraction. Specifically, the new sources will spur a much greater integration of structure and dynamics considerations for all classes of material, including disordered and heterogeneous materials.

For current information on and links to major X-ray facilities and instrumentation around the world please see <http://www.lightsources.org/regions>.

## 5.8. DISORDERED HETEROGENEOUS MATERIALS

### 5.8.4.2. *Developments at steady-state and pulsed neutron sources*

While neutron fluxes are never likely to match those possible with X-rays, the high penetration ability in most materials, the absence of sample beam damage and the strong isotope effect for neutron scattering present major advantages for studies of disordered and heterogeneous materials. The magnetic properties of neutrons, and also their sensitivity to inelastic processes in materials, also provide important advantages. As pulsed (spallation) neutron sources have been developed around the world in recent years, the field of neutron powder diffraction has advanced significantly (Ibberson, 2009; Garlea *et al.*, 2010). The availability of long-pulse operations at an increasing number of locations together with the construction of long-flight-path instruments have enabled major advances in neutron total-scattering measurements and, to some degree, combination of WANS with SANS within the same instrument configuration (White *et al.*, 2010; Bowron *et al.*, 2010). Meanwhile, at steady-state (reactor-based) neutron sources, the greater availability of cold neutrons and the ability to achieve higher signal-to-noise ratios for SANS continue to make reactors the prime location for dedicated SANS measurement. Recent innovations in neutron optics such as neutron refractive lenses, new detector developments and the development of successful USANS instruments are resulting in new emerging SANS capabilities, such as the ability to measure in several instrument configurations at once (Frielinghaus *et al.*, 2009; Huang *et al.*, 2012). This will greatly reduce sample measurement times and improve the time resolution for *in situ* studies of material processes. Indeed, reactor-based SANS measurements continue to lead the exploration of *in situ* processes in polymer systems and other disordered materials (Eberle & Porcar, 2012).

For current information on and links to major steady-state reactor and pulsed source neutron facilities and instrumentation around the world please see <http://www.neutron.anl.gov/facilities.html>.

### 5.8.4.3. *Future prospects*

In closing we note that advanced technological materials development is increasingly concerned with harnessing complex phenomena in multi-component and heterogeneous material systems. The materials involved are frequently a hybrid mix of alloys, polymers and ceramics, intimately connected for the intended purpose of the overall system. Many of the material components are nanoscale and/or nanocrystalline in nature, or have poor crystallinity, or none. Even if not disordered with regard to crystalline structure, disordered distributions of heterogeneous elements are frequently present, and they may even govern performance. While many of the techniques and practices described elsewhere in this volume are appropriate for providing the needed characterization of new material systems, we have attempted in this chapter to focus on suitable methods for characterizing and measuring their more disordered aspects.

### 5.8.4.4. *Further reading*

Some selected textbooks relevant to the methods described in this chapter are listed below in chronological order.

Guinier, A. & Fournet, G. (1955). *Small-Angle Scattering of X-rays*. New York: John Wiley & Sons.

Kostorz, G. (1979). Editor. *Treatise on Materials Science and Technology*, Vol. 15, *Neutron Scattering*. New York: Academic Press.

Glatter, O. & Kratky, O. (1982). Editors. *Small-Angle X-ray Scattering*. London: Academic Press.

Feigin, L. A. & Svergun, D. I. (1987). *Structure Analysis by Small-Angle X-ray and Neutron Scattering*. New York: Plenum Press.

Brumberger, H. (1994, reprinted 2010). Editor. *Modern Aspects of Small-Angle Scattering*. NATO Science Series, Series C, *Mathematical and Physical Sciences*, 451. London: Springer.

Roe, R.-J. (1999). *Methods of X-ray and Neutron Scattering in Polymer Science*. Don Mills, ON, Canada: Oxford University Press (Canada).

Lindner, P. & Zemb, Th. (2002). Editors. *Neutron, X-ray & Light Scattering Methods Applied to Soft Condensed Matter*. Amsterdam: North Holland Delta Series.

Andersson, R. A. (2008). *Spin-echo Small-Angle Neutron Scattering Measurements*. Berlin, Heidelberg: Springer.

Borsali, R. & Pecora, R. (2008). Editors. *Soft Matter Characterization*. Berlin, Heidelberg: Springer.

Daillant, J. & Gibaud, A. (2009). Editors. *X-ray and Neutron Reflectivity: Principles and Applications. Lecture Notes in Physics* Vol. 770. Berlin, Heidelberg: Springer.

Egami, T. & Billinge, S. (2012). *Underneath the Bragg Peaks*. Oxford: Pergamon Press.

The SAS Portal web site, linked to the web site of the IUCr Commission on Small-Angle Scattering, includes a list of references and other educational links, not only for SAS methods, but also for general scattering methods relevant to heterogeneous materials in general – see <http://smallangle.org/content/small-angle-scattering-bibliography>.

## References

- Agamalian, M., Wignall, G. D. & Triolo, R. (1997). *Optimization of a Bonse–Hart ultra-small-angle neutron scattering facility by elimination of the rocking-curve wings*. *J. Appl. Cryst.* **30**, 345–352.
- Allen, A. J. (1991). *Time-resolved phenomena in cements, clays and porous rocks*. *J. Appl. Cryst.* **24**, 624–634.
- Allen, A. J. (2005). *Characterization of ceramics by X-ray and neutron small-angle scattering*. *J. Am. Ceram. Soc.* **88**, 1367–1381.
- Allen, A. J., Gavillet, D. & Weertman, J. R. (1993). *SANS and TEM studies of isothermal M<sub>2</sub>C carbide precipitation in ultrahigh strength AF1410 steels*. *Acta Metall. Mater.* **41**, 1869–1884.
- Allen, A. J., Ilavsky, J., Jemian, P. R. & Braun, A. (2014). *Evolution of electrochemical interfaces in solid oxide fuel cells (SOFC): a Ni and Zr resonant anomalous ultra-small-angle X-ray scattering study with elemental and spatial resolution across the cell assembly*. *RSC Adv.* **4**, 4676–4690.
- Allen, A. J., Thomas, J. J. & Jennings, H. M. (2007). *Composition and density of nanoscale calcium-silicate-hydrate in cement*. *Nat. Mater.* **6**, 311–316.
- Allen, A. J., Zhang, F., Kline, R. J., Guthrie, W. F. & Ilavsky, J. (2017). *NIST Standard Reference Material 3600: absolute intensity calibration standard for small-angle X-ray scattering*. *J. Appl. Cryst.* **50**, 462–474.
- Als-Nielsen, J. (2001). *Elements of Modern X-ray Physics*. New York: John Wiley & Sons.
- Andersson, R. A. (2008). *Spin-Echo Small-Angle Neutron Scattering Measurements*. Berlin, Heidelberg: Springer.
- Babonneau, D. (2010). *FitGISAXS: software package for modelling and analysis of GISAXS data using IGOR Pro*. *J. Appl. Cryst.* **43**, 929–936.
- Bale, H. D. & Schmidt, P. W. (1984). *Small-angle X-ray-scattering investigation of submicroscopic porosity with fractal properties*. *Phys. Rev. Lett.* **53**, 596–599.
- Barker, J. G., Glinka, C. J., Moyer, J. J., Kim, M. H., Drews, A. R. & Agamalian, M. (2005). *Design and performance of a thermal-neutron double-crystal diffractometer for USANS at NIST*. *J. Appl. Cryst.* **38**, 1004–1011.

## 5. DEFECTS, TEXTURE AND MICROSTRUCTURE

- Bates, S., Zografi, G., Engers, D., Morris, K., Crowley, K. & Newman, A. (2006). *Analysis of amorphous and nanocrystalline solids from their X-ray diffraction patterns*. *Pharm. Res.* **23**, 2333–2349.
- Beaucage, G. (1995). *Approximations leading to a unified exponential/power-law approach to small-angle scattering*. *J. Appl. Cryst.* **28**, 717–728.
- Becker, J., Bremholm, M., Tyrsted, C., Pauw, B., Jensen, K. M. Ø., Eltzholt, J., Christensen, M. & Iversen, B. B. (2010). *Experimental setup for in situ X-ray SAXS/WAXS/PDF studies of the formation and growth of nanoparticles in near- and supercritical fluids*. *J. Appl. Cryst.* **43**, 729–736.
- Berk, N. F. & Hardman-Rhyne, K. A. (1985). *Characterization of alumina powder using multiple small-angle neutron scattering. I. Theory*. *J. Appl. Cryst.* **18**, 467–472.
- Berk, N. F. & Hardman-Rhyne, K. A. (1988). *Analysis of SAS data dominated by multiple scattering*. *J. Appl. Cryst.* **21**, 645–651.
- Billinge, S. J. L. & Levin, I. (2007). *The problem with determining atomic structure at the nanoscale*. *Science*, **316**, 561–565.
- Bonse, U. & Hart, M. (1966). *Small angle X-ray scattering by spherical particles of polystyrene and polyvinyltoluene*. *Z. Phys.* **189**, 151–162.
- Borsali, R. & Pecora, R. (2008). Editors. *Soft Matter Characterization*. Berlin, Heidelberg: Springer.
- Bowron, D. T., Soper, A. K., Jones, K., Ansell, S., Birch, S., Norris, J., Perrott, L., Riedel, D., Rhodes, N. J., Botti, A., Ricci, M.-A., Grazi, F. & Zoppi, M. (2010). *NIMROD: The Near and Intermediate Range Order Diffractometer of the ISIS second target station*. *Rev. Sci. Instrum.* **81**, 033905.
- Brumberger, H. (1994, reprinted 2010). Editor. *Modern Aspects of Small-Angle Scattering*. NATO Science Series, Series C, *Mathematical and Physical Sciences*, 451. London: Springer.
- Cargill, G. S. (1971). *Influence of neglected small-angle scattering in radial distribution function analysis*. *J. Appl. Cryst.* **4**, 277–283.
- Cromer, D. T. & Liberman, D. (1970). *Relativistic calculation of anomalous scattering factors for X rays*. *J. Chem. Phys.* **53**, 1891–1898.
- Dailant, J. & Gibaud, A. (2009). Editors. *X-ray and Neutron Reflectivity: Principles and Applications*. *Lecture Notes in Physics*, Vol. 770. Berlin, Heidelberg: Springer.
- De Teresa, J. M., Ibarra, M. R., Algarabel, P. A., Ritter, C., Marquina, C., Blasco, J., García, J., del Moral, A. & Arnold, Z. (1997). *Evidence for magnetic polarons in the magnetoresistive perovskites*. *Nature*, **386**, 256–259.
- Debye, P. (1947). *Molecular weight determination by light scattering*. *J. Phys. Colloid Chem.* **51**, 18–32.
- Debye, P. & Bueche, A. M. (1949). *Scattering by an inhomogeneous solid*. *J. Appl. Phys.* **20**, 518–525.
- Eberle, A. P. R. & Porcar, L. (2012). *Flow-SANS and Rheo-SANS applied to soft matter*. *Curr. Opin. Colloid Interface Sci.* **17**, 33–43.
- Eikenberry, E. F., Bronnimann, Ch., Hulsen, G., Toyokawa, H., Horisberger, R., Schmitt, B., Schulze-Briese, C. & Tomizaki, T. (2003). *PILATUS: a two-dimensional X-ray detector for macromolecular crystallography*. *Nucl. Instrum. Methods Phys. Res. A*, **501**, 260–266.
- Egami, T. & Billinge, S. (2012). *Underneath the Bragg Peaks*. Oxford: Pergamon Press.
- Emmerling, A. & Fricke, J. (1992). *Small-angle scattering and the structure of aerogels*. *J. Non-Cryst. Sol.* **145**, 113–120.
- Espinal, L., Wong-Ng, W., Kaduk, J. A., Allen, A. J., Snyder, C. R., Chiu, C., Siderius, D. W., Li, L., Cockayne, E., Espinal, A. E. & Suib, S. L. (2012). *Time-dependent CO<sub>2</sub> sorption hysteresis in a one-dimensional microporous octahedral molecular sieve*. *J. Am. Chem. Soc.* **134**, 7944–7951.
- Farrow, C. L. & Billinge, S. J. L. (2009). *Relationship between the atomic pair distribution function and small-angle scattering: implications for modeling of nanoparticles*. *Acta Cryst.* **A65**, 232–239.
- Feigin, L. A. & Svergun, D. I. (1987). *Structure Analysis by Small-Angle X-ray and Neutron Scattering*. New York: Plenum Press.
- Fratzl, P. (2003). *Small-angle scattering in materials science – a short review of applications in alloys, ceramics and composite materials*. *J. Appl. Cryst.* **36**, 397–404.
- Freltoft, T., Kjems, J. K. & Sinha, S. K. (1986). *Power-law correlations and finite-size effects in silica particle aggregates studied by small-angle neutron scattering*. *Phys. Rev. B*, **33**, 269–275.
- Frielinghaus, H., Pipich, V., Radulescu, A., Heiderich, M., Hanslik, R., Dahlhoff, K., Iwase, H., Koizumi, S. & Schwahn, D. (2009). *Aspherical refractive lenses for small-angle neutron scattering*. *J. Appl. Cryst.* **42**, 681–690.
- Garlea, V. O., Chakoumakos, B. C., Moore, S. A., Taylor, G. B., Chae, T., Maples, R. G., Riedel, R. A., Lynn, G. W. & Selby, D. L. (2010). *The high-resolution powder diffractometer at the high flux isotope reactor*. *Appl. Phys. A*, **99**, 531–535.
- Glatter, O. (1977). *A new method for the evaluation of small-angle scattering data*. *J. Appl. Cryst.* **10**, 415–421.
- Glatter, O. (1980). *Determination of particle-size distribution functions from small-angle scattering data by means of the indirect transformation method*. *J. Appl. Cryst.* **13**, 7–11.
- Glatter, O. & Kratky, O. (1982). Editors. *Small-Angle X-ray Scattering*. London: Academic Press.
- Glatter, O. & May, R. (2006). *Small-angle techniques*. In *International Tables for Crystallography*, Vol. C, Chapter 2.6, pp. 89–112. Chester: International Union of Crystallography.
- Glinka, C. J., Barker, J. G., Hammouda, B., Krueger, S., Moyer, J. J. & Orts, W. J. (1998). *The 30 m small-angle neutron scattering instruments at the National Institute of Standards and Technology*. *J. Appl. Cryst.* **31**, 430–445.
- Green, D. L., Lin, J. S., Lam, Y.-F., Hu, M. Z.-C., Schaefer, D. W. & Harris, M. T. (2003). *Size, volume fraction, and nucleation of Stober silica nanoparticles*. *J. Colloid Interface Sci.* **266**, 346–358.
- Green, M. L., Allen, A. J., Jordan-Sweet, J. L. & Ilavsky, J. (2009). *Annealing behavior of atomic layer deposited HfO<sub>2</sub> films studied by synchrotron X-ray reflectivity and grazing incidence small-angle scattering*. *J. Appl. Phys.* **105**, 103522.
- Grillo, I. (2008). *Small-angle neutron scattering and applications in soft condensed matter*. In *Soft Matter Characterization*, edited by R. Borsali & R. Pecora, pp. 707–764. Berlin, Heidelberg: Springer Verlag.
- Guinier, A. & Fournet, G. (1955). *Small-Angle Scattering of X-rays*. New York: John Wiley & Sons.
- Hamilton, W. A., Butler, P. D., Hayter, J. B., Magid, L. J. & Kreke, P. J. (1996). *‘Over the horizon’ SANS: measurements on near-surface Poiseuille shear-induced ordering of dilute solutions of threadlike micelles*. *Physica B*, **221**, 309–319.
- Heinemann, A. & Wiedenmann, A. (2003). *Benefits of polarized small-angle neutron scattering on magnetic nanometer scale structure modeling*. *J. Appl. Cryst.* **36**, 845–849.
- Hoyt, J. J., de Fontaine, D. & Warburton, W. K. (1984). *Determination of the anomalous scattering factors for Cu, Ni and Ti using the dispersion relation*. *J. Appl. Cryst.* **17**, 344–351.
- Huang, T. C., Gong, H., Shao, B. B., Wang, D., Zhang, X. Z., Zhang, K., Wei, J., Wang, X. W., Guan, X. L., Loong, C.-K., Tao, J. Z., Zhou, L. & Ke, Y. B. (2012). *Design of a new time-of-flight small-angle neutron scattering instrument at CPHS*. *Nucl. Instrum. Methods Phys. Res. A*, **669**, 14–18.
- Hyeon-Lee, J., Beaucage, G., Pratsinis, S. E. & Vemury, S. (1998). *Fractal analysis of flame-synthesized nanostructured silica and titania powders using small-angle X-ray scattering*. *Langmuir*, **14**, 5751–5756.
- Ibberson, R. M. (2009). *Design and performance of the new supermirror guide on HRPD at ISIS*. *Nucl. Instrum. Methods Phys. Res. A*, **600**, 47–49.
- Ibel, K. (1976). *The neutron small-angle camera D11 at the high-flux reactor, Grenoble*. *J. Appl. Cryst.* **9**, 296–309.
- Ilavsky, J. (2012). *Nika: software for two-dimensional data reduction*. *J. Appl. Cryst.* **45**, 324–328.
- Ilavsky, J., Allen, A. J., Levine, L. E., Zhang, F., Jemian, P. R. & Long, G. G. (2012). *High-energy ultra-small-angle X-ray scattering instrument at the Advanced Photon Source*. *J. Appl. Cryst.* **45**, 469–479.
- Ilavsky, J., Jemian, P. R., Allen, A. J., Zhang, F., Levine, L. E. & Long, G. G. (2009). *Ultra-small-angle X-ray scattering at the Advanced Photon Source*. *J. Appl. Cryst.* **42**, 1318–1320.
- Jennings, H. M. (2000). *A model for the microstructure of calcium silicate hydrate in cement paste*. *Cem. Concr. Res.* **30**, 101–116.
- Jouault, N., Vallat, P., Dalmas, F., Said, S., Jestin, J. & Boue, F. (2009). *Well-dispersed fractal aggregates as filler in polymer-silica nanocomposites: long-range effects in rheology*. *Macromolecules*, **42**, 2031–2040.
- Juhás, P., Davis, T., Farrow, C. L. & Billinge, S. J. L. (2013). *PDFgetX3: a rapid and highly automatable program for processing powder diffraction data into total scattering pair distribution functions*. *J. Appl. Cryst.* **46**, 560–566.
- Keen, D. A. & Goodwin, A. L. (2015). *The crystallography of correlated disorder*. *Nature*, **521**, 303–309.

## 5.8. DISORDERED HETEROGENEOUS MATERIALS

- Kline, S. R. (2006). *Reduction and analysis of SANS and USANS data using IGOR Pro*. *J. Appl. Cryst.* **39**, 895–900.
- Korolkov, D., Busch, P., Willner, L., Kentzinger, E., Rucker, U., Paul, A., Frielinghaus, H. & Brückel, T. (2012). *Analysis of randomly oriented structures by grazing-incidence small-angle neutron scattering*. *J. Appl. Cryst.* **45**, 245–254.
- Kostorz, G. (1979). Editor. *Treatise on Materials Science and Technology*, Vol. 15, *Neutron Scattering*, pp. 227–287. New York: Academic Press.
- Lai, Y.-H., Sun, Y.-S., Jeng, U.-S., Lin, J.-M., Lin, T.-L., Sheu, H.-S., Chuang, W.-T., Huang, Y.-S., Hsu, C.-H., Lee, M.-T., Lee, H.-Y., Liang, K. S., Gabriel, A. & Koch, M. H. J. (2006). *An instrument for time-resolved and anomalous simultaneous small- and wide-angle X-ray scattering (SWAXS) at NSRRC*. *J. Appl. Cryst.* **39**, 871–877.
- Lake, J. A. (1967). *An iterative method of slit-correcting small angle X-ray data*. *Acta Cryst.* **23**, 191–194.
- Lazzari, R. (2002). *ISGISAXS: a program for grazing-incidence small-angle X-ray scattering analysis of supported islands*. *J. Appl. Cryst.* **35**, 406–421.
- Levine, J. R., Cohen, J. B. & Chung, Y. W. (1991). *Thin film island growth kinetics: a grazing incidence small angle X-ray scattering study of gold on glass*. *Surf. Sci.* **248**, 215–224.
- Lindner, P. & Zemb, Th. (2002). Editors. *Neutron, X-ray & Light Scattering Methods Applied to Soft Condensed Matter*. Amsterdam: North Holland Delta Series.
- Long, G. G., Jemian, P. R., Weertman, J. R., Black, D. R., Burdette, H. E. & Spal, R. (1991). *High-resolution small-angle X-ray scattering camera for anomalous scattering*. *J. Appl. Cryst.* **24**, 30–37.
- Mathon, M. H., de Carlan, Y., Geoffroy, G., Averty, X., Alamo, A. & de Novion, C. H. (2003). *A SANS investigation of the irradiation-enhanced  $\alpha$ - $\alpha'$  phases separation in 7–12 Cr martensitic steels*. *J. Nucl. Mater.* **312**, 236–248.
- Mettus, D. & Michels, A. (2015). *Small-angle neutron scattering correlation functions of bulk magnetic materials*. *J. Appl. Cryst.* **48**, 1437–1450.
- Mezei, F. (1980). *Neutron Spin Echo*. *Lecture Notes in Physics*, Vol. 128. Berlin, Heidelberg: Springer.
- Moor, P. E. A. de, Beelen, T. P. M., Komanschek, B. U., Diat, O. & van Santen, R. A. (1997). *In situ investigation of Si-TPA-MFI crystallization using (ultra-) small- and wide-angle X-ray scattering*. *J. Phys. Chem. B*, **101**, 11077–11086.
- Morrison, J. D., Corcoran, J. D. & Lewis, K. E. (1992). *The determination of particle size distributions in small-angle scattering using the maximum-entropy method*. *J. Appl. Cryst.* **25**, 504–513.
- Mullen, K. & Levin, I. (2011). *Mitigation of errors in pair distribution function analysis of nanoparticles*. *J. Appl. Cryst.* **44**, 788–797.
- Nelson, A. (2006). *Co-refinement of multiple-contrast neutron/X-ray reflectivity data using MOTOFIT*. *J. Appl. Cryst.* **39**, 273–276.
- Parratt, L. G. (1954). *Surface studies of solids by total reflection of X-rays*. *Phys. Rev.* **95**, 359–369.
- Pauly, T. R., Liu, Y., Pinnavaia, T. J., Billinge, S. J. L. & Rieker, T. P. (1999). *Textural mesoporosity and the catalytic activity of mesoporous molecular sieves with wormhole framework structures*. *J. Am. Chem. Soc.* **121**, 8835–8842.
- Pedersen, J.-S. (1997). *Analysis of small-angle scattering data from colloids and polymer solutions: modeling and least-squares fitting*. *Adv. Colloid Interface Sci.* **70**, 171–210.
- Pedersen, J. S. (2000). *Form factors of block copolymer micelles with spherical, ellipsoidal and cylindrical cores*. *J. Appl. Cryst.* **33**, 637–640.
- Percus, J. K. & Yevick, G. J. (1958). *Analysis of classical statistical mechanics by means of collective coordinates*. *Phys. Rev.* **110**, 1–13.
- Petkov, V., Ren, Y., Kabekkodu, S. & Murphy, D. (2013). *Atomic pair distribution functions analysis of disordered low-Z materials*. *Phys. Chem. Chem. Phys.* **15**, 8544–8554.
- Ponchut, C. (2006). *Characterization of X-ray area detectors for synchrotron beamlines*. *J. Synchrotron Rad.* **13**, 195–203.
- Porod, G. (1951). *X-ray low angle scattering of dense colloid systems, part I*. *Kolloid Z.* **124**, 83–114.
- Porod, G. (1952). *X-ray low angle scattering of dense colloid systems, part II*. *Kolloid Z.* **125**, 108–122.
- Potton, J. A., Daniell, G. J. & Rainford, B. D. (1988). *Particle size distributions from SANS data using the maximum entropy method*. *J. Appl. Cryst.* **21**, 663–668.
- Price, D. L. (1999). *Neutron scattering from disordered materials*. *J. Neutron Res.* **7**, 247–258.
- Proffen, T., Billinge, S. J. L., Egami, T. & Louca, D. (2003). *Structural analysis of complex materials using the atomic pair distribution function – a practical guide*. *Z. Kristallogr.* **218**, 132–143.
- Proffen, T. & Kim, H. (2009). *Advances in total scattering analysis*. *J. Mater. Chem.* **19**, 5078–5088.
- Rauscher, M., Salditt, T. & Spohn, H. (1995). *Small-angle X-ray scattering under grazing incidence: the cross section in the distorted-wave Born approximation*. *Phys. Rev. B*, **52**, 16855–16863.
- Rekvelde, M. T. (1996). *Novel SANS instrument using neutron spin echo*. *Nucl. Instrum. Methods Phys. Res. B*, **114**, 366–370.
- Renteria, A. F., Saruhan, B., Ilavsky, J. & Allen, A. J. (2007). *Application of USAXS analysis and non-interacting approximation to determine the influence of process parameters and ageing on the thermal conductivity of electron-beam physical vapor deposited thermal barrier coatings*. *Surf. Coat. Technol.* **201**, 4781–4788.
- Riseman, T. M., Kealey, P. G., Forgan, E. M., Mackenzie, A. P., Galvin, L. M., Tyler, A. W., Lee, S. L., Ager, C., Paul, D., Aegerter, C. M., Cubitt, R., Mao, Z. Q., Akima, T. & Maeno, Y. (1998). *Observation of a square flux-line lattice in the unconventional superconductor  $\text{Sr}_2\text{RuO}_4$* . *Nature*, **396**, 242–245.
- Ritter, C., Ibarra, M. I., De Teresa, J. M., Algarabel, P. A., Marquina, C., Blasco, J., Garcia, J., Oseroff, S. & Cheong, S.-W. (1997). *Influence of oxygen content on the structural, magnetotransport, and magnetic properties of  $\text{LaMnO}_{3+\delta}$* . *Phys. Rev. B*, **56**, 8902–8911.
- Roe, R.-J. (1999). *Methods of X-ray and Neutron Scattering in Polymer Science*. Don Mills: Oxford University Press (Canada).
- Roess, L. C. & Shull, C. G. (1947). *X-ray scattering at small angles by finely-divided solids. II. Exact theory for random distributions of spheroidal particles*. *J. Appl. Phys.* **18**, 308–313.
- Roux, J.-N., Broseta, B. & Deme, B. (2001). *SANS study of asphaltene aggregation: concentration and solvent quality effects*. *Langmuir*, **17**, 5085–5092.
- Saldin, D. K., Poon, H. C., Bogan, M. J., Marchesini, S., Shapiro, D. A., Kirian, R. A., Weierstall, U. & Spence, J. C. H. (2011). *New light on disordered ensembles: ab initio structure determination of one particle from scattering fluctuations of many copies*. *Phys. Rev. Lett.* **106**, 115501.
- Schelten, J. & Schmatz, W. (1980). *Multiple-scattering treatment for small-angle scattering problems*. *J. Appl. Cryst.* **13**, 385–390.
- Scherrenberg, R., Coussens, B., van Vliet, P., Edouard, G., Brackman, J., de Brabander, E. & Mortensen, K. (1998). *The molecular characteristics of poly(propyleneimine) dendrimers as studied with small-angle neutron scattering, viscosimetry and molecular dynamics*. *Macromolecules*, **31**, 456–461.
- Schwahn, D., Miksovsky, A., Rauch, H., Seidl, E. & Zugarek, G. (1985). *Test of channel-cut perfect crystals for neutron small angle scattering experiments*. *Nucl. Instrum. Methods Phys. Res. A*, **239**, 229–234.
- Sears, V. F. (1992). *Neutron scattering lengths and cross sections*. *Neutron News*, **3**, 26–37.
- Shull, C. G. & Roess, L. C. (1947). *X-ray scattering at small angles by finely-divided solids. I. General approximate theory and applications*. *J. Appl. Phys.* **18**, 295–307.
- Sinha, S. K., Sirota, E. B., Garoff, S. & Stanley, H. B. (1988). *X-ray and neutron scattering from rough surfaces*. *Phys. Rev. B*, **38**, 2297–2311.
- Spieler, H. (2008). *Semiconductor Detector Systems*. Oxford University Press.
- Tavares, P. F., Leemann, S. C., Sjoström, M. & Andersson, A. (2014). *The MAX IV storage ring project*. *J. Synchrotron Rad.* **21**, 862–877.
- Thompson, A. (2009). Editor. *X-ray Data Booklet*. Publication PUB-490 Rev. 3. Berkeley: Lawrence Berkeley National Laboratory.
- Toby, B. H. & Egami, T. (1992). *Accuracy of pair distribution function analysis applied to crystalline and non-crystalline materials*. *Acta Cryst.* **A48**, 336–346.
- Wagner, W., Wiedenmann, A., Petry, W., Geibel, A. & Gleiter, H. (1991). *Magnetic microstructure of nanostructured Fe, studied by small angle neutron scattering*. *J. Mater. Res.* **6**, 2305–2311.
- Warren, B. E. (1990). *X-ray Diffraction*. New York: Dover.
- White, C. E., Provis, J. L., Proffen, T., Riley, D. P. & van Deventer, J. S. J. (2010). *Combining density functional theory (DFT) and pair distribution function (PDF) analysis to solve the structure of metastable materials: the case of metakaolin*. *Phys. Chem. Chem. Phys.* **12**, 3239–3245.
- Wilson, K. S., Allen, A. J., Washburn, N. R. & Antonucci, J. M. (2007). *Interphase effects in dental nanocomposites investigated by small-angle neutron scattering*. *J. Biomed. Mater. Res. A*, **81**, 113–123.

## 5. DEFECTS, TEXTURE AND MICROSTRUCTURE

- Yaron, U., Gammel, P. L., Huse, D. A., Kleiman, R. N., Oglesby, C. S., Bucher, E., Batlogg, B., Bishop, D. J., Mortensen, K. & Clausen, K. N. (1995). *Structural evidence for a two-step process in the depinning of the superconducting flux-line lattice*. *Nature*, **376**, 753–755.
- Zhang, F., Allen, A. J., Levine, L. E., Ilavsky, J., Long, G. G. & Sandy, A. R. (2011). *Development of ultra-small-angle X-ray scattering–X-ray photon correlation spectroscopy*. *J. Appl. Cryst.* **44**, 200–212.
- Zhao, J. K., Gao, C. Y. & Liu, D. (2010). *The extended Q-range small-angle neutron scattering diffractometer at the SNS*. *J. Appl. Cryst.* **43**, 1068–1077.
- Zhao, J., Meerwinck, W., Niinikoski, T., Rijllart, A., Schmitt, M., Willumeit, R. & Stuhmann, H. (1995). *The polarized target station at GKSS*. *Nucl. Instrum. Methods Phys. Res. A*, **356**, 133–137.